Shock Waves (2019) 29:1155–1179
https://doi.org/10.1007/s00193-019-00915-1

ORIGINAL ARTICLE

Nonlinear subscale turbulent models for very large eddy simulation of turbulent flows

T.-H. Shih[1] · J. P. Moder[2] · N.-S. Liu[2]

Received: 15 November 2018 / Revised: 10 June 2019 / Accepted: 15 July 2019 / Published online: 27 August 2019

Abstract
A brief introduction of the time-filtered Navier–Stokes (TFNS) equations for very large eddy simulation (VLES) and its distinct features is presented. A set of nonlinear subscale models and their advantages over the linear subscale eddy viscosity models are described. A guideline for conducting a TFNS/VLES simulation is also provided. In this paper, we present simulations for three turbulent flows. The first one is the turbulent pipe flow at both low and high Reynolds numbers to illustrate the basic features of TFNS/VLES; the second one is the swirling turbulent flow in an LM6000 single injector to further demonstrate the differences between the results from nonlinear models versus linear viscosity models; the third one is a more complex turbulent flow generated in a single-element lean direct injection combustor, which demonstrates that the current TFNS/VLES approach is capable of predicting dynamically important, unsteady turbulent structures even with a relatively coarse mesh grid.

Keywords Turbulence · Very large eddy simulations · Time-filtered

1 Introduction

Many engineering applications of computational fluid dynamics (CFD) for turbulent flows need to capture relatively large scales of unsteady turbulent structures at both low and high Reynolds numbers to facilitate a higher-fidelity analysis of the design. The conventional Reynolds-averaged Navier–Stokes (RANS) approach is known to be limited for this kind of task, because the RANS solution does not contain the above-mentioned flow information. Recently, an approach called TFNS [1, 2] has been developed for simulations of very large-scale turbulence, which only requires a relatively coarse mesh grid that is often used in a RANS simulation. Although TFNS is mainly aimed at very large eddy simulations, hence named as TFNS/VLES, it can easily be extended to perform large eddy simulation (LES) when the grid spacing reaches the resolution of traditional LES. The approach of TFNS/VLES is based on the concept of time-filtering to avoid the frequently overlooked issues that the traditional LES approach (based on the spatial filter of mesh grid) suffers from when a nonuniform mesh grid is used in the simulation. In TFNS/VLES, the larger time scales (or lower frequencies) of the turbulence are directly calculated and the effects of the unresolved time scales of the turbulence are modeled by nonlinear subscale models. The contents of both resolved and unresolved turbulence are regulated by a resolution control parameter (RCP), which is related to the width of the time-filter. In the development of the TFNS/VLES approach, it was named as the partially resolved numerical simulation (PRNS) and this name will appear on many figures in this paper.

The basic equations of TFNS/VLES and subscale models are grid invariant, i.e., they are totally independent of the mesh grid. Therefore, it is possible to achieve a grid-independent numerical solution, and this is one of the major differences from the traditional LES approach. (Note that the exact equations of traditional LES and their subscale models are dependent on the grid spacing.) Another distinction is that TFNS/VLES enables us to perform unsteady RANS (URANS),

Communicated by C.-H. Chang.

Electronic supplementary material The online version of this article (https://doi.org/10.1007/s00193-019-00915-1) contains supplementary material, which is available to authorized users.

✉ T.-H. Shih
thshih@sbcglobal.net

[1] Ohio Aerospace Institute, Brook Park, OH 44142, USA

[2] NASA Glenn Research Center, Cleveland, OH 44135, USA

VLES, LES, and even DNS in a unified way through a judicious selection of the value of the RCP, in conjunction with the employment of a grid spacing whose numerical resolution can consistently support the scale contents stipulated by the selected RCP.

It should be noted that the TFNS/VLES approach is not a variant of the popular hybrid RANS/LES [3–6]. There is no enforced transition between the perceived RANS and LES domains.

The subscale model is always one of the key issues in all turbulent numerical simulations. Some less-than-satisfactory simulations using the Smagorinsky eddy viscosity and its variants have been reported in the past [7, 8]. Recently, we have also noticed that using a linear model, the TFNS/VLES was unable to successfully simulate the turbulent pipe flow at a low Reynolds number $\mathrm{Re}_\tau = 180$ (based on the pipe radius and the skin friction velocity). During the calculation, the turbulent fluctuations were not sustainable over a long period of time and were eventually suppressed. This is attributable to the attempt of just using the eddy viscosity to account for all the subscale effects, even though the eddy viscosity is constructed from a k–ε dynamic equation system. It is known that, in addition to the dissipative and diffusive effects accounted for through the eddy viscosity, the effects of anisotropy and rotation should also be included in the subscale model, especially when the simulation is for very large scales of turbulence. To construct a more general relationship between the unresolved turbulent stresses and the resolved turbulent flow field, we have followed the analysis of the rational mechanics and obtained a general constitutive relationship [9, 10]. This relationship indeed shows that, in addition to an eddy viscosity term, there are several other terms representing the anisotropy and the rotation effects due to the interactions between the resolved and unresolved turbulence. They then introduce source terms in the momentum equations to sustain the turbulent fluctuations in the calculated flow field. The simulations presented in this paper will demonstrate this unique feature of the nonlinear subscale models.

In the following, a brief description of the TFNS/VLES equations and the nonlinear subscale models will first be presented, followed by an outline for the concurrent selections of RCP and the numerical mesh grid. The results of simulations from three turbulent flows are then presented: the turbulent pipe flow, the turbulent swirling flow issued from an LM6000 single injector, and the flow generated in a single-element LDI combustor.

2 Time-filter-based TFNS/VLES approach

Using a homogeneous time-filter $G(t-t')$, the large time-scale turbulent variable denoted as $\overline{\phi}$ and its density-weighted variable $\widetilde{\phi}$ can be defined as

$$\bar{\phi}(t,x_i) = \int \phi(t',x_i) G(t-t')\,\mathrm{d}t',$$
$$\widetilde{\phi} = \frac{\overline{\rho\phi}}{\bar{\rho}} = \frac{1}{\bar{\rho}} \int \rho(t',x_i)\,\phi(t',x_i)\,G(t-t')\,\mathrm{d}t', \tag{1}$$

where the integral is over the entire time domain and the time-filter G satisfies the normalization condition: $\int G(t-t')\,\mathrm{d}t' = 1$. There are several such time-filters available; the simplest one is the top-hat filter:

$$G(t-t') = \begin{cases} 1/\Delta_\mathrm{T}, & \text{if } |t-t'| \le \Delta_\mathrm{T}/2 \\ 0, & \text{otherwise} \end{cases}, \tag{2}$$

where Δ_T is the width of the top-hat filter. For a homogeneous time-filter, Δ_T is a constant and independent of the space. Using this filter, the left part of (1) becomes

$$\bar{\phi}(t,x_i) = \frac{1}{\Delta_\mathrm{T}} \int_{t-\Delta_\mathrm{T}/2}^{t+\Delta_\mathrm{T}/2} \phi(t',x_i)\,\mathrm{d}t'. \tag{3}$$

Equation (3) reveals a unified feature of $\bar{\phi}$ and $\tilde{\phi}$, because they will become the exact Reynolds-averaged quantity and Favre-averaged quantity when $\Delta_\mathrm{T} \to \infty$. On the other hand, they will become the instantaneous turbulent quantity as $\Delta_\mathrm{T} \to 0$. For a finite Δ_T, they represent the quantities of large time-scale turbulence.

2.1 Basic equations

Performing the filtering operation defined by (1) on the Navier–Stokes equations, we obtain a set of exact, basic equations for the resolved, large time-scale turbulence ($\bar{\phi}$ and $\tilde{\phi}$):

$$\left(\bar{\rho}\tilde{u}_i\right)_{,t} + \left(\bar{\rho}\tilde{u}_i\tilde{u}_j\right)_{,j} = -\bar{p}_{,i} - \tau_{ij,j} + \left(2\bar{\mu}\tilde{s}_{ij} - \frac{2}{3}\delta_{ij}\bar{\mu}\tilde{s}_{kk}\right)_{,j}, \tag{4}$$

$$\left(\bar{\rho}\widetilde{e}\right)_{,t} + \left(\bar{\rho}\tilde{u}_i\tilde{e}\right)_{,i} = \left(\bar{\kappa}\tilde{T}_{,i}\right)_{,i} + \overline{ps_{kk}} - q_{i,i} + \left(2\bar{\mu}\widetilde{s_{ij}s_{ij}} - \frac{2}{3}\bar{\mu}\widetilde{s_{kk}s_{ii}}\right) + \overline{Q}, \tag{5}$$

$$\bar{\rho}_{,t} + \left(\bar{\rho}\tilde{u}_i\right)_{,i} = 0, \quad \bar{p} = \bar{\rho}R\tilde{T}, \tag{6}$$

$$\tau_{ij} \equiv \bar{\rho}(\widetilde{u_iu_j} - \tilde{u}_i\tilde{u}_j), \quad q_i \equiv \bar{\rho}(\widetilde{u_ie} - \tilde{u}_i\tilde{e}), \tag{7}$$

where $s_{ij} = \left(u_{i,j} + u_{j,i}\right)/2$. The symbols $()_{,t}$ and $()_{,i}$ represent the temporal and spatial derivatives, respectively. ρ, u_i, T, p, e, and Q are the density, velocity, temperature, pressure, internal energy per unit mass, and the radiation rate. μ and κ are the viscosity and heat conductivity of the fluid. R is the universal gas constant. τ_{ij} and q_i are the extra unknown terms that were created by processing the time-filtered Navier–Stokes equations. They represent the effects

of unresolved time-scale turbulence. They are not in closed forms and must be modeled. We call them the unresolved (or subscale) turbulent stresses and heat fluxes.

It is clear that the basic equations (4)–(7), which govern the large time-scale turbulence, are not associated with the mesh grid; hence, they are grid invariant. This feature should be maintained in the development of subscale models.

It is important to note that in the time-filtered turbulent field, the time-filter width Δ_T (considered as a resolvable smallest time scale) is not the only factor in determining the smallest resolvable length scale of the simulated turbulence, and this leaves room for arranging the grid spacing to carry out a physically meaningful numerical simulation.

2.2 Nonlinear subscale models

In order to obtain the solution for the large time-scale turbulence using TFNS/VLES (4)–(6), we must model the unclosed terms defined in (7): $\tau_{ij} \equiv \bar{\rho}(u_i u_j - \tilde{u}_i \tilde{u}_j)$, $q_i \equiv \bar{\rho}(u_i e - \tilde{u}_i \tilde{e})$. There are several ways to model these terms. The more sophisticated method is to directly solve the transport equations for the subscale turbulent stresses and heat fluxes, which can be derived from the Navier–Stokes equations (see [1]). This method will require models for some higher-order unclosed terms (for example, the pressure–strain correlations, etc.) that appeared in the transport equations of τ_{ij} and q_i. A less complicated way is based on the rational mechanics to establish some general constitutive relationships between the unresolved turbulent quantities (τ_{ij}, q_i) and the resolved large time-scale turbulent quantities $\tilde{s}_{ij}$, $\tilde{\omega}_{ij}$, and $\tilde{e}_{,i}$. These general constitutive relationships are then simplified according to the flow complexity by truncating the higher-order nonlinear terms of $\tilde{s}_{ij}$, $\tilde{\omega}_{ij}$, and $\tilde{e}_{,i}$. For example, the simplest form is just a linear relationship, which is the widely used conventional subscale eddy viscosity model. Even at this level, there are several ways to formulate the subscale eddy viscosity. The most popular one used in the traditional LES is the Smagorinsky model [11] and its variations, which explicitly uses the local grid spacing Δ as the filtering length scale. A more sophisticated one is the one-equation model, such as the one proposed by Kim and Menon [12], which solves the transport equation of the unresolved turbulent kinetic energy k, and uses $\sqrt{k}$ as the velocity scale of unresolved turbulence, and at the same time keeps the local grid spacing as the filtering length scale.

In the context of TFNS/VLES, the subscale model is required to be a function of the width of the time-filter Δ_T, but independent of the local grid spacing. The constitutive relationship for the subscale turbulent stresses is derived from a general constitutive relationship [13] by invoking the realizability condition and the rapid distortion theory limit. The current nonlinear subscale model contains linear, quadratic, and cubic terms, while the time-filter width Δ_T appears via the resolution control parameter (RCP), see (14).

2.2.1 Modeling of subscale turbulent stresses τ_{ij}

The model proposed for TFNS/VLES is the following:

$$\begin{aligned}\tau_{ij} &= -2f_1 C_\mu \bar{\rho}\frac{k^2}{\varepsilon}\left(\tilde{s}_{ij} - \delta_{ij}\tilde{s}_{kk}/3\right) + \frac{2}{3}f_1\bar{\rho}k\delta_{ij} \\ &\quad - A_3 f_3 \bar{\rho}\frac{k^3}{\varepsilon^2}\left(\tilde{s}_{ik}\tilde{\omega}_{kj} - \tilde{\omega}_{ik}\tilde{s}_{kj}\right) \\ &\quad + 2A_5 f_5 \bar{\rho}\frac{k^4}{\varepsilon^3}\Big[\tilde{\omega}_{ik}\tilde{s}_{kj}^2 - \tilde{s}_{ik}^2\tilde{\omega}_{kj} + \tilde{\omega}_{ik}\tilde{s}_{km}\tilde{\omega}_{mj} \\ &\quad - \tilde{\omega}_{kl}\tilde{s}_{lm}\tilde{\omega}_{mk}\delta_{ij}/3 + II_s(\tilde{s}_{ij} - \delta_{ij}\tilde{s}_{kk}/3)\Big],\end{aligned} \tag{8}$$

where $\tilde{s}_{ij} = \left(\tilde{u}_{i,j} + \tilde{u}_{j,i}\right)/2$, $\tilde{\omega}_{ij} = \left(\tilde{u}_{i,j} - \tilde{u}_{j,i}\right)/2$ $II_s = \left(\tilde{s}_{kk}\tilde{s}_{mm} - \tilde{s}_{kl}\tilde{s}_{lk}\right)/2$. The model coefficients C_μ, A_3, and A_5 are constrained by the realizability condition and the rapid distortion theory limit. They are formulated as (see [13]):

$$C_\mu = \frac{1}{4.0 + A_s\frac{k}{\varepsilon}U^*}, \quad A_3 = \frac{\sqrt{1.0 - A_s^2 C_\mu^2\left(\frac{k}{\varepsilon}S^*\right)^2}}{0.5 + 1.5\frac{k^2}{\varepsilon^2}\Omega^* S^*}, \quad A_5 = \frac{1.6C_\mu\bar{\rho}\frac{k^2}{\varepsilon}}{\bar{\rho}\frac{k^4}{\varepsilon^3}\frac{7S^*S^* + \Omega^*\Omega^*}{4}}, \tag{9}$$

in which

$$A_s = \sqrt{6}\cos\varphi, \quad \varphi = \frac{1}{3}\arccos\left(\sqrt{6}W^*\right), \quad W^* = \frac{S_{ij}^* S_{jk}^* S_{ki}^*}{(S^*)^3}, \tag{10}$$

$$U^* = \sqrt{(S^*)^2 + (\Omega^*)^2}, \quad S^* = \sqrt{S_{ij}^* S_{ij}^*}, \quad \Omega^* = \sqrt{\omega_{ij}\omega_{ij}}, \quad S_{ij}^* = \tilde{s}_{ij} - \frac{1}{3}\delta_{ij}\tilde{s}_{kk}. \tag{11}$$

The coefficients f_1, f_3, and f_5 are functions of Δ_T/T, i.e., the ratio of the time-filter width to the global time scale of the turbulent flow of interest, where the global time scale T can be considered as the maximum integral time scale in the entire domain. These functions should have the following property:

$$f_i\left(\frac{\Delta_T}{T}\right) = \begin{cases} 0 & \text{if } \frac{\Delta_T}{T} \to 0, \\ 1 & \text{if } \frac{\Delta_T}{T} \to 1. \end{cases} \tag{12}$$

This is because the subscale turbulent stresses τ_{ij} must vanish when the filter width Δ_T vanishes, and τ_{ij} must approach the Reynolds stresses R_{ij} as Δ_T increases toward the global time scale T. In TFNS/VLES, $\Delta_T/T < 1$, so we may take the following general expansion:

$$f_i\left(\frac{\Delta_T}{T}\right) = C_0^i + C_1^i\left(\frac{\Delta_T}{T}\right) + C_2^i\left(\frac{\Delta_T}{T}\right)^2 + \cdots \quad i = 1, 3, 5. \tag{13}$$

All C_0^i must be zero, because f_i must be zero as Δ_T goes to zero. If we retain the two leading terms as an approximation and assume the first-order derivative of f_i is zero at $\Delta_T/T = 1$ to reflect that f_i reaches its maximum value of 1.0 at $\Delta_T/T = 1$, then all f_i will have the same form:

$$f_i\left(\frac{\Delta_T}{T}\right) \approx 2\left(\frac{\Delta_T}{T}\right) - \left(\frac{\Delta_T}{T}\right)^2 \quad i = 1, 3, 5 \tag{14}$$

We call the ratio Δ_T/T the resolution control parameter (RCP). It controls, at the governing equation level, the content of resolved large time-scale turbulence in the resolved field, which may, in theory, contain all length scales that have not been physically filtered. However, at the numerical solution level, the grid spacing will be imposed, and the solution (say, the subscale eddy viscosity ν_T) together with the RCP will determine the content of resolved large-length scale turbulence. We will further discuss this parameter in Sect. 2.3.

2.2.2 Physics of nonlinear interaction between resolved and unresolved turbulence

It is important to identify the various physical interactions between the resolved and unresolved turbulent scales and to understand how these interactions are mimicked in the numerical simulation. In the momentum equation (4), these interactions are represented by the term $\tau_{ij,j}$, which is unclosed and must be modeled. In the traditional LES, this term is modeled via the isotropic eddy viscosity. Therefore, the effect of the interactions is accounted for only by a modification to the viscosity of the fluid. However, the real physical interactions are much more complex than this. In fact, according to the general constitutive relationship τ_{ij} contains many more terms, in addition to a leading term that is related to an eddy viscosity. For example, the model of τ_{ij} in (8) has two parts: the linear term and the nonlinear (quadratic and cubic) terms. Each part plays a different role in the momentum equations. The linear part leads to a term acting like an additional viscosity called subscale eddy viscosity, and the nonlinear part leads to terms acting like additional sources promoting the resolved large-scale turbulence. This can be clearly demonstrated by plugging the τ_{ij} model into (4), which yields

$$\left(\bar{\rho}\tilde{u}_i\right)_{,t} + \left(\bar{\rho}\tilde{u}_i\tilde{u}_j\right)_{,j} = -\bar{p}_{,i} + \left(2\left(\bar{\mu} + \mu_T\right)\tilde{s}_{ij} - \frac{2}{3}\delta_{ij}\left(\bar{\mu} + \mu_T\right)\tilde{s}_{kk}\right)_{,j} + S_i^T, \tag{15}$$

where

$$\mu_T \equiv f_1 C_\mu \bar{\rho}\frac{k^2}{\varepsilon} \tag{16}$$

$$S_i^T = -\frac{2}{3}\left(f_1\bar{\rho}k\right)_{,i} + \left\{A_3 f_3 \bar{\rho}\frac{k^3}{\varepsilon^2}\left(\tilde{s}_{ik}\tilde{\omega}_{kj} - \tilde{\omega}_{ik}\tilde{s}_{kj}\right)\right\}_{,j} - \left\{2A_5 f_5 \bar{\rho}\frac{k^4}{\varepsilon^3}\left[\tilde{\omega}_{ik}\tilde{s}_{kj}^2 - \tilde{s}_{ik}^2\tilde{\omega}_{kj} + \tilde{\omega}_{ik}\tilde{s}_{km}\tilde{\omega}_{mj} - \tilde{\omega}_{kl}\tilde{s}_{lm}\tilde{\omega}_{mk}\delta_{ij}/3 + II_s(\tilde{s}_{ij} - \delta_{ij}\tilde{s}_{kk}/3)\right]\right\}_{,j}. \tag{17}$$

Apparently, the linear part of the model adds an additional subscale eddy viscosity μ_T (which is isotropic) to the viscosity of the fluid $\bar{\mu}$; and the nonlinear part provides a complex source term S_i^T that accounts for the effects of anisotropy and rotation.

We have noticed that, although different subscale eddy viscosity models have been used in different LES approaches, most of them have neglected or missed the source term S_i^T. Our study shows that this source term could become critically important for some flow simulations, especially for those at relatively low Reynolds numbers or flows with strong rotation, and this will be demonstrated in Sects. 3.1.1.2 and 3.2.2.

2.2.3 Transport equations for subscale *k* and *ε*

To complete the proposed model for τ_{ij}, we need k and ε, the unresolved (or subscale) turbulent kinetic energy and its dissipation rate. Their exact transport equations can be derived from the Navier–Stokes equations and contain several higher-order unclosed terms due to the time-filtering operation. Here, we briefly describe the procedure of the derivation. The first step is to establish the transport equation for τ_{ij}, followed by a tracing operation to establish the equation for τ_{ii} (which is $2\bar{\rho}\,k$), and this leads to the transport equation for k.

The exact transport equation for the subscale turbulent stresses τ_{ij} (i.e., $\widetilde{\bar{\rho}u_iu_j} - \bar{\rho}\tilde{u}_i\tilde{u}_j$) is

$$\tau_{ij,t} + \left(\tilde{u}_k\tau_{ij}\right)_{,k} = D_{ij} + \Phi_{ij} + P_{ij} - \bar{\rho}\varepsilon_{ij}, \tag{18}$$

where D_{ij}, Φ_{ij}, P_{ij}, and $\bar{\rho}\varepsilon_{ij}$ are the diffusion term, the pressure–strain correlation term, the production term, and the dissipation term, respectively. The following expressions indicate that all terms on the right-hand side of the equation, except for the production term P_{ij}, are unclosed and must be modeled.

$$
\begin{aligned}
D_{ij} &= -\left(\widetilde{\bar{\rho}\bar{u}_i\bar{u}_j\bar{u}_k} - \widetilde{\bar{\rho}\bar{u}_i\bar{u}_j}\,\tilde{u}_k\right) \\
&\quad + \left\{2\bar{\mu}\widetilde{\bar{u}_j\bar{s}_{ik}} - \frac{2}{3}\delta_{ik}\bar{\mu}\widetilde{\bar{u}_j\bar{s}_{mm}} - \left[\widetilde{u}_j\left(2\bar{\mu}\bar{s}_{ik} - \frac{2}{3}\delta_{ik}\bar{\mu}\bar{s}_{mm}\right)\right]\right\}_{,k} \\
&\quad + \left(\tau_{ik}\tilde{u}_j + \tau_{jk}\tilde{u}_i\right)_{,k} - \left(\widetilde{\bar{p}\bar{u}_j}\delta_{ik} + \widetilde{\bar{p}\bar{u}_i}\delta_{jk} - \bar{p}\tilde{u}_j\delta_{ik} - \bar{p}\tilde{u}_i\delta_{jk}\right)_{,k} \\
&\quad + \left\{2\bar{\mu}\widetilde{\bar{u}_i\bar{s}_{jk}} - \frac{2}{3}\delta_{jk}\bar{\mu}\widetilde{\bar{u}_i\bar{s}_{mm}} - \left[\tilde{u}_i\left(2\bar{\mu}\bar{s}_{jk} - \frac{2}{3}\delta_{jk}\bar{\mu}\bar{s}_{mm}\right)\right]\right\}_{,k} \\
\Phi_{ij} &= 2\widetilde{\bar{p}\bar{s}_{ij}} - 2\bar{p}\tilde{s}_{ij} \\
P_{ij} &= -\tau_{ik}\tilde{u}_{j,k} - \tau_{jk}\tilde{u}_{i,k} \\
\bar{\rho}\varepsilon_{ij} &= \left[2\bar{\mu}\left(\widetilde{\bar{s}_{ik}\bar{u}_{j,k}} + \widetilde{\bar{s}_{jk}\bar{u}_{i,k}}\right) - \frac{4}{3}\bar{\mu}\widetilde{\bar{s}_{mm}\bar{s}_{ij}}\right] \\
&\quad - \left[2\bar{\mu}\left(\tilde{s}_{ik}\tilde{u}_{j,k} + \tilde{s}_{jk}\tilde{u}_{i,k}\right) - \frac{4}{3}\bar{\mu}\tilde{s}_{mm}\tilde{s}_{ij}\right].
\end{aligned}
$$

Now, if the diffusion term D_{ij} is modeled by a gradient-type diffusion of τ_{ij} with the effective viscosity $\bar{\mu} + \mu_{\mathrm{T}}$, then the trace of (18) becomes the following equation of subscale turbulent kinetic energy k:

$$
\frac{\partial}{\partial t}\bar{\rho}k + \frac{\partial}{\partial x_i}\bar{\rho}\tilde{u}_i k = \frac{\partial}{\partial x_i}\left[\left(\bar{\mu} + \mu_{\mathrm{T}}\right)\frac{\partial}{\partial x_i}k\right] - \tau_{ij}\tilde{s}_{ij} - \bar{\rho}\varepsilon, \tag{19}
$$

in which Φ_{ii} has been neglected by ignoring the effect of compressibility on τ_{ii}. The term of subscale dissipation rate $\bar{\rho}\,\varepsilon$ is defined by $\bar{\rho}\,\varepsilon_{ii}/2$, i.e.,

$$
\bar{\rho}\varepsilon = \left(2\bar{\mu}\widetilde{\bar{s}_{ij}\bar{s}_{ij}} - \frac{2}{3}\bar{\mu}\widetilde{\bar{s}_{mm}\bar{s}_{ii}}\right) - \left(2\bar{\mu}\tilde{s}_{ij}\tilde{s}_{ij} - \frac{2}{3}\bar{\mu}\widetilde{\bar{s}_{mm}}\widetilde{\bar{s}_{ii}}\right). \tag{20}
$$

A model transport equation for the dissipation rate ε can be constructed by the analogy to (19) as

$$
\frac{\partial}{\partial t}\bar{\rho}\varepsilon + \frac{\partial}{\partial x_i}\bar{\rho}\tilde{u}_i\varepsilon = \frac{\partial}{\partial x_i}\left[\left(\bar{\mu} + \mu_{\mathrm{T}}\right)\frac{\partial}{\partial x_i}\varepsilon\right] - C_{\varepsilon 1}\tau_{ij}\tilde{s}_{ij}\frac{\varepsilon}{k} - C_{\varepsilon 2}\frac{\bar{\rho}\varepsilon^2}{k}, \tag{21}
$$

where $C_{\varepsilon 1}$ and $C_{\varepsilon 2}$ are the model coefficients. We have adopted the commonly used values of $C_{\varepsilon 1} = 1.45$ and $C_{\varepsilon 2} = 1.92$ in the present work, while keeping in mind that they can be further constructed as functions of the local subscale turbulence quantities [14].

2.2.4 Modeling of subscale turbulent heat fluxes q_i

A common practice in modeling the unresolved turbulent heat fluxes $q_i \equiv \bar{\rho}(\widetilde{\bar{u}_i\bar{e}} - \tilde{u}_i\tilde{e})$ is to employ the following isotropic model:

$$
q_i = -\kappa_{\mathrm{T}}\tilde{e}_{,i}, \tag{22}
$$

where κ_{T} is the eddy diffusivity for the heat, which is often modeled as $\kappa_{\mathrm{T}} = \mu_{\mathrm{T}}/\,\mathrm{Pr}_{\mathrm{T}}$, where Pr_{T} (about 0.9) is the turbulent Prandtl number. However, based on the analysis of the constitutive relationship (see [9, 10]), the simplest form that considers the effects of strain and rotation should be

$$
q_i = -\kappa_{\mathrm{T}}\tilde{e}_{,i} - \kappa_{\mathrm{T}}\frac{k}{\varepsilon}\left(c_1\tilde{s}_{ij} + c_2\tilde{\omega}_{ij}\right)\tilde{e}_{,j}, \tag{23}
$$

where c_1 and c_2 are yet-to-be-determined coefficients. This more general model will result in modifications to both the diffusion term and the source term in (5):

$$
\begin{aligned}
\left(\bar{\rho}\tilde{e}\right)_{,t} + \left(\bar{\rho}\tilde{u}_i\tilde{e}\right)_{,i} &= \left(\left(\bar{\kappa} + \kappa_{\mathrm{T}}\right)\tilde{e}_{,i}\right)_{,i} + \widetilde{\bar{p}\bar{s}_{kk}} + \left(2\bar{\mu}\widetilde{\bar{s}_{ij}\bar{s}_{ij}} - \frac{2}{3}\bar{\mu}\widetilde{\bar{s}_{kk}\bar{s}_{ii}}\right) \\
&\quad + \overline{Q} + S_{\mathrm{T}}^{\mathrm{e}},
\end{aligned} \tag{24}
$$

where the extra source term that originated from the unresolved turbulent heat fluxes is

$$
S_{\mathrm{T}}^{\mathrm{e}} = \left[\kappa_{\mathrm{T}}\frac{k}{\varepsilon}\left(c_1\tilde{s}_{ij} + c_2\tilde{\omega}_{ij}\right)\tilde{e}_{,j}\right]_{,i}. \tag{25}
$$

So far, all common RANS and LES simulations have missed this source term. Based on our previous studies, we set $c_1 = c_2 = -0.24$ in the simulations described in Sect. 3.

2.3 Guideline for conducting simulations

In the unfiltered turbulent flow field, the smallest time, length, and velocity scales are the Kolmogorov micro-scales [15], which are determined by the viscosity of fluid and the turbulent dissipation rate. For the time-filtered turbulent flow field, by invoking an analogy to the Kolmogorov micro-scales, we may estimate that the subscales of time, length, and velocity for the unresolved turbulence should be determined by the effective subscale viscosity $(\nu_{\mathrm{T}} + \bar{\mu}/\bar{\rho})$ and subscale turbulent dissipation rate ε as follows:

$$
\begin{aligned}
\tau_{\mathrm{TFNS}} &= \left(\frac{\nu_{\mathrm{T}} + \bar{\mu}/\,\bar{\rho}}{\varepsilon}\right)^{\frac{1}{2}}, \quad \eta_{\mathrm{TFNS}} = \left(\frac{\left(\nu_{\mathrm{T}} + \bar{\mu}/\,\bar{\rho}\right)^3}{\varepsilon}\right)^{\frac{1}{4}}, \\
\upsilon_{\mathrm{TFNS}} &= \left[\left(\nu_{\mathrm{T}} + \bar{\mu}/\,\bar{\rho}\right)\varepsilon\right]^{\frac{1}{4}},
\end{aligned} \tag{26}
$$

where $\nu_{\mathrm{T}} \equiv \mu_{\mathrm{T}}/\,\bar{\rho}$, which is the subscale eddy viscosity. Following (26), the relationship between the length subscale η_{TFNS} and the time subscale $_{\mathrm{TFNS}}$ is

$$
\eta_{\mathrm{TFNS}} = \left[\tau_{\mathrm{TFNS}}\left(\nu_{\mathrm{T}} + \bar{\mu}/\,\bar{\rho}\right)\right]^{\frac{1}{2}}. \tag{27}
$$

Equation (27) indicates that for a given time subscale τ_{TFNS} (its value should be the width of time-filter Δ_{T}), the length subscale η_{TFNS} will automatically adjust itself to the change of subscale eddy viscosity ν_{T}, or vice versa, i.e., the subscale eddy viscosity ν_{T} will adjust itself to a given local grid spacing that usually defines the value of the length subscale η_{TFNS}. In this sense, there is a flexibility when selecting the grid spacing for a given time-filter width. However, the

situation may occur that for a given Δ_T, the ν_T is no longer changing as the local grid spacing is reducing, which means that the simulation reaches a grid-independent solution, and the length subscale η_{TFNS} is no longer decreasing as local grid spacing is reducing.

2.3.1 Resolution control parameter (RCP)

The resolution control parameter (RCP) (i.e., the ratio Δ_T/T) is used in TFNS/VLES to regulate the content of the time scales of the resolved turbulence. When RCP $\rightarrow 1.0$, all time scales of turbulent fluctuation have been filtered and the TFNS/VLES simulation becomes a RANS simulation. As the value of RCP decreases, the turbulent fluctuations become more pronounced in the calculated flow field and the simulation moves toward VLES or LES.

To carry out a very large eddy simulation, we need to choose a value of RCP from the outset. As we mentioned previously that the time-filter width Δ_T is of the same order of τ_{TFNS}. Therefore, by using (26), we have

$$\Delta_T = \left(\frac{\nu_T + \bar{\mu}/\bar{\rho}}{\varepsilon} \right)^{\frac{1}{2}} \approx \frac{k}{\varepsilon}. \tag{28}$$

This is based on the assumption that $\nu_T \gg \bar{\mu}/\bar{\rho}$ for a very large eddy simulation and the subscale eddy viscosity ν_T is of order k^2/ε, where k and ε are the subscale kinetic energy and its dissipation rate. As a result, the resolution control parameter (RCP) (Δ_T/T) is estimated according to

$$\text{RCP} = \frac{\Delta_T}{T} \sim \frac{k/\varepsilon}{k_{ref}/\varepsilon_{ref}} \sim \frac{k}{k_{ref}}, \tag{29}$$

where T is the global time scale of turbulent flow of interest and is expressed as a ratio of the reference turbulent kinetic energy to its dissipation rate. We have also assumed that ε_{ref} and ε are of the same order, since the dissipation mostly occurs in the small scales [15]. Equation (29) suggests a way to guide the selection of the value of RCP. For example, RCP = 0.20 means that we intend to directly resolve those turbulent scales that are responsible for about 80% of the total turbulent kinetic energy while modeling the rest of the unresolved turbulent scales that contain about 20% of the total turbulent kinetic energy.

In the simulations presented in Sect. 3, all the mesh grids are given mostly from the previous RANS simulations. The coefficient $f(\Delta_T/T)$ for the subscale model in (8) is set to RCP = 0.16, 0.18, and 0.25 for the pipe flow, the LM6000 injector, and the LDI combustor, respectively. The above settings mean that the TFNS/VLES simulation is to resolve the large-scale turbulence that contains about 84% of the total turbulent kinetic energy for the pipe flow, 82% for the LM6000 injector, and 75% for the LDI combustor.

2.3.2 Arrangement of numerical mesh grid and possible grid-independent solution

A computational mesh grid based on a priori knowledge of the flow field is generated subject to the constraint of the available computing resources. Typically, finer grid spacing is used in regions where the shear rates are higher and the turbulent fluctuations are stronger. Then we decide the extent to which the turbulence is to be resolved. In general, simulations with different levels of coarse grid spacing are all legitimate. And of course, the finer turbulent structures will reveal the finer grid spacing, but the statistical mean should be about the same. By refining the grid, it is possible to attain a grid-independent solution and η_{TFNS} would remain the same order of magnitude when the grid spacing is further reduced.

3 Numerical results of TFNS/VLES simulations

The simulations of three turbulent flows will be presented: The first one is a turbulent pipe flow to illustrate the basic features of TFNS/VLES; the second one is a swirling turbulent flow in a GE LM6000 single injector to further demonstrate the advantage of the nonlinear subscale models over the common eddy viscosity models; and the third one is a nonreacting flow in a single-element lean direct injection (LDI) combustor. The last simulation was performed with a relatively coarse grid for a quite complex geometry; its important dynamical, unsteady turbulent flow structures have been well observed.

3.1 Pipe flows

The turbulent pipe flow is one of the ideal benchmark flows for evaluating/validating numerical simulation approaches, because the geometry is simple and the flow is statistically homogeneous in the axial direction so that periodic boundary conditions can be applied to the inlet and the outlet to avoid the often-complicated boundary condition issues. In addition, some experimental data [16] are available for comparison.

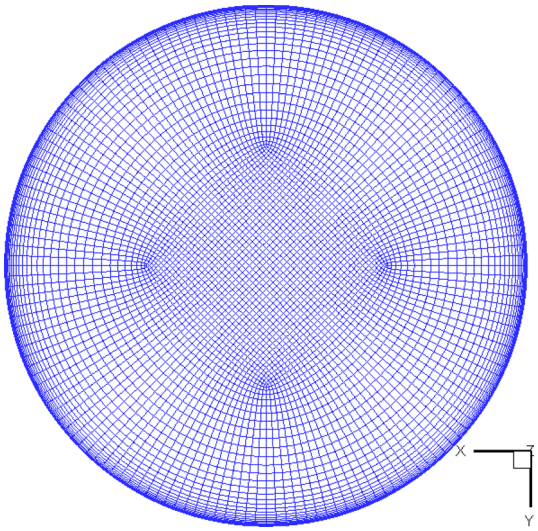

Fig. 1 Grid spacing in a cross section of the pipe

Turbulent pipe flows at several different Reynolds numbers (from high to low) have been used to evaluate the fundamentals of the TFNS/VLES approach [17]. At each Reynolds number, the simulation was performed over a range of *f*(RCP) (from 0.2 to 1.0) to demonstrate the unified feature of the current approach. Also, two types of subscale models were used for flow simulation at each Reynolds number: One is a traditional linear eddy viscosity model, and the other is a nonlinear subscale model described by (8). We have found that the nonlinear subscale model is critically important for the successful simulation of low-Reynolds-number pipe flow. Here we present some results at two Reynolds numbers: $\mathrm{Re}_\tau = 180$ and 3322 (based on the pipe radius and friction velocity). The value of RCP was set to 0.16, which is a typical value for a very large eddy simulation.

The computational domain has an aspect ratio of length/radius = 10, where radius = 0.06468 m. Figure 1 shows the grid spacing in a cross section of the pipe. The grid is nearly orthogonal everywhere. The total number of the hexahedral elements is 906,750, more specifically $(156\times 29+39\times 39)\times 150$.

This grid was used for flows at both Reynolds numbers 180 and 3322. The initial flow field was created by an arbitrary smooth profile plus random fluctuation. At the wall, a generalized wall function was imposed [18].

3.1.1 Reynolds number $\mathrm{Re}_\tau = 180$

Turbulent pipe flow at the low Reynolds number $\mathrm{Re}_\tau = 180$ (or Re = 7000 based on the pipe diameter and centerline velocity) is relatively weak. In this section, we will present the numerical results, which demonstrate that for such a low-Reynolds-number turbulent flow, the linear eddy viscosity subscale model is unable to develop and sustain turbulent fluctuations in the numerical simulation.

3.1.1.1 Nonlinear subscale model The time history of the velocity indicates that the initially induced random fluctuations are significantly damped during the first 600 time-steps, but the new fluctuations quickly grow and evolve into a fully developed turbulence (see Fig. 2a, b).

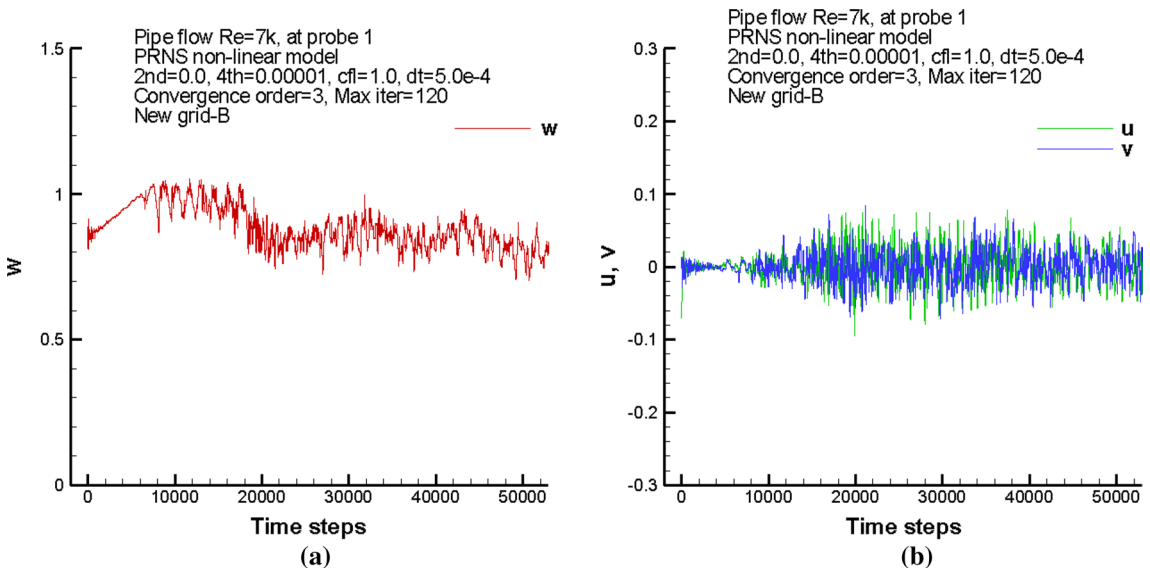

Fig. 2 Time history of **a** axial velocity; **b** *u*, *v* components

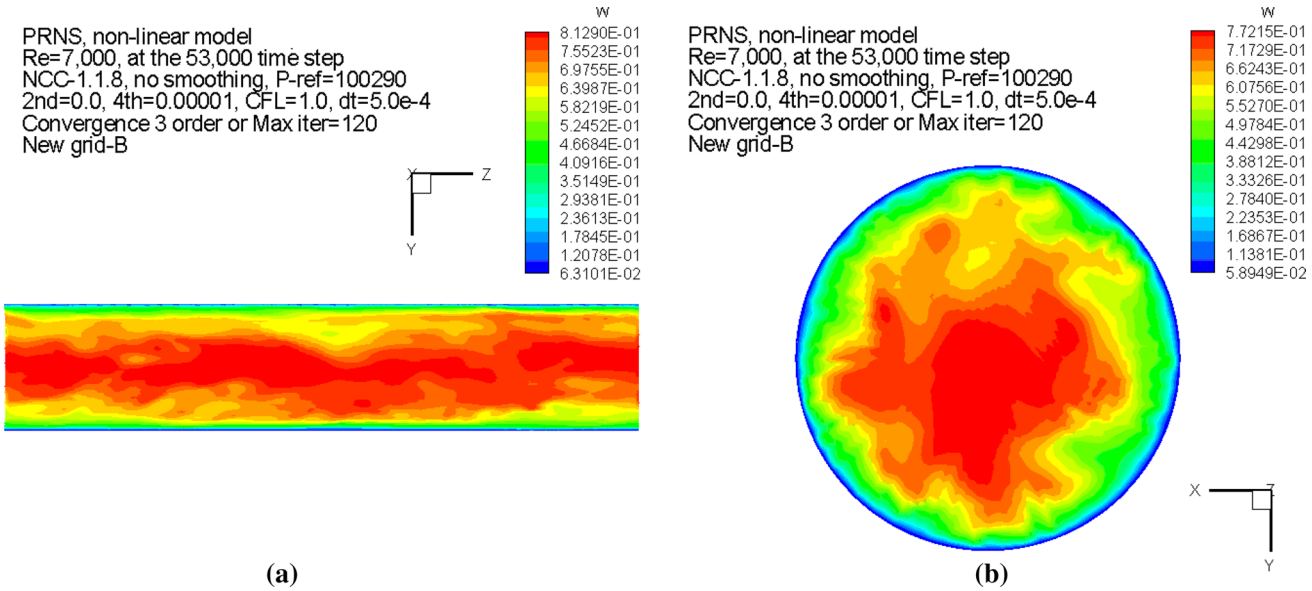

Fig. 3 Instantaneous contours of axial velocity in **a** a center plane; **b** a cross section

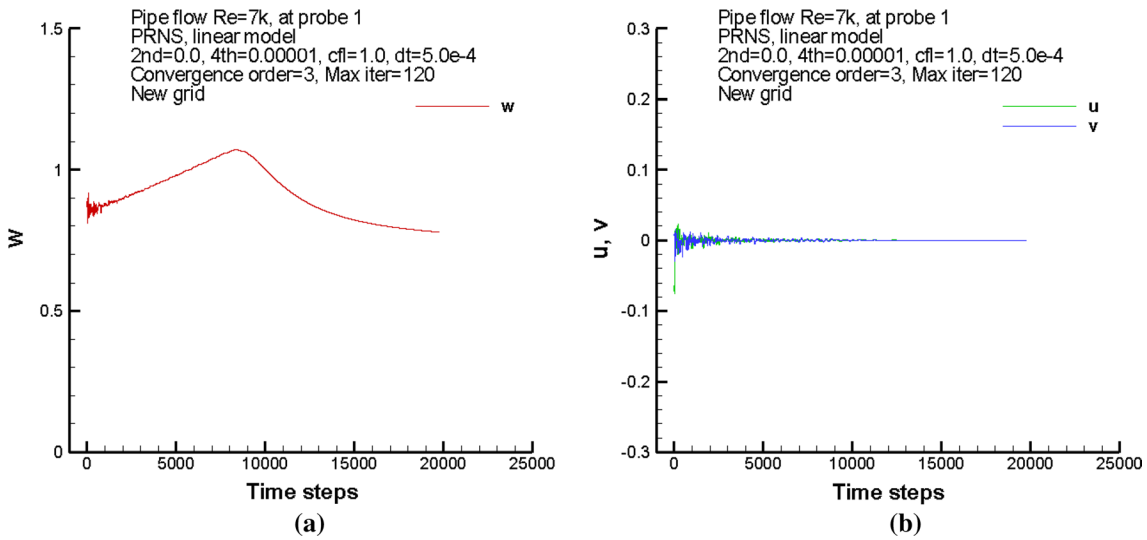

Fig. 4 Time history of **a** the axial velocity w; **b** the velocity components u, v

The instantaneous contours of the axial velocity in a center plane (Fig. 3a) and in a cross section (Fig. 3b) clearly demonstrate the motions of various turbulent scales.

3.1.1.2 Linear subscale model The TFNS/VLES with a linear eddy viscosity subscale model is unable to perform the fluctuation of a fully developed turbulent pipe flow. The time histories of the three velocity components w, u, and v at the center of the pipe indicate that the initially induced random fluctuations are quickly damped out and no new turbulent fluctuation develops (see Fig. 4a, b).

Figure 5a, b shows the contours of the axial velocity in a center plane and a cross section of the pipe, respectively. These smooth contours do not show any turbulent fluctuations.

To further study these phenomena, we have restarted a simulation using the eddy viscosity subscale model but starting from a fully developed turbulent flow field obtained in Sect. 3.1.1.1. We have observed that this initial fully developed turbulence was not able to be sustained and the turbulent fluctuation was quickly damped out. Then we continued the simulation by turning on the nonlinear subscale model;

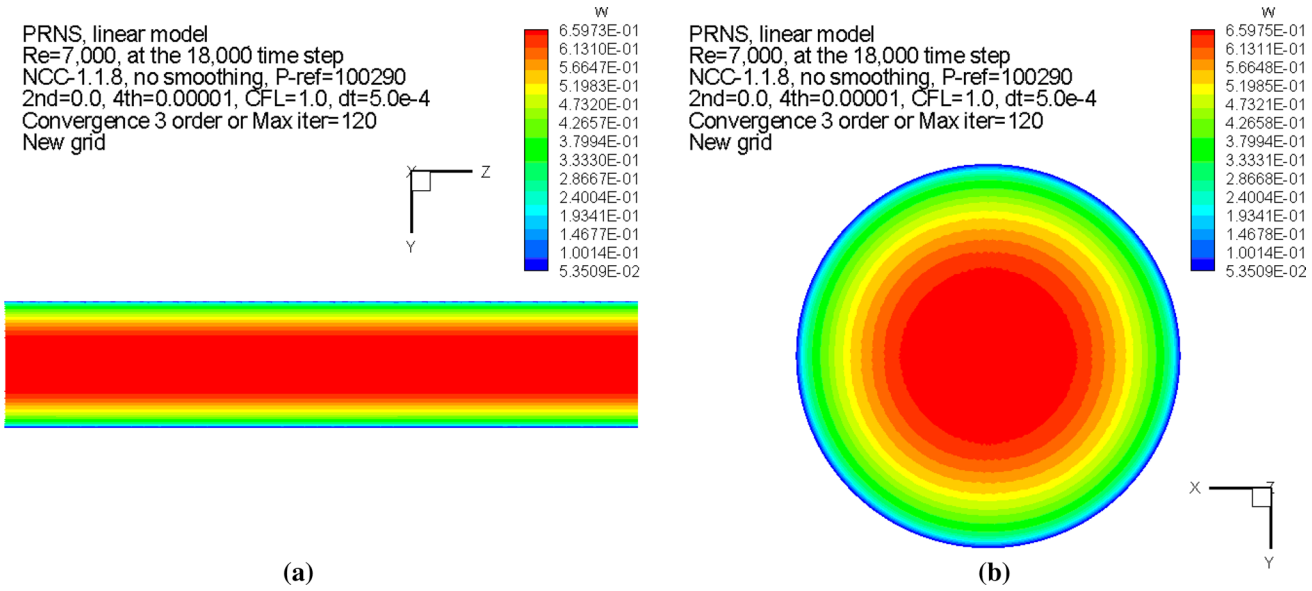

Fig. 5 Contours of w component in **a** a center plane; **b** a cross section

we found that the turbulent fluctuations were quickly developing and evolving into a fully developed turbulent pipe flow. The above simulations suggest that the linear eddy viscosity model is not suitable for the TFNS/VLES simulation of a low-Reynolds-number turbulent flow.

3.1.2 Reynolds number $Re_\tau = 3322$

Turbulent pipe flow at high Reynolds number $Re_\tau = 3322$ (or $Re = 150{,}000$ based on the pipe diameter and centerline velocity) has quite strong turbulence. The strong turbulent fluctuations are easy to sustain in the numerical simulation even with a linear eddy viscosity subscale model. We have performed simulations using RCP = 0.16 with both linear and nonlinear subscale models. In both cases, the initially induced random fluctuations were able to evolve into the fully developed turbulent fluctuations. Here we only present the numerical results from using the nonlinear subscale model.

3.1.2.1 Time history The time histories of the velocity components w, u, v, and the subscale turbulent kinetic energy are recorded at 15 probes at various radial locations at the axial center of the pipe. We present the time histories of the axial

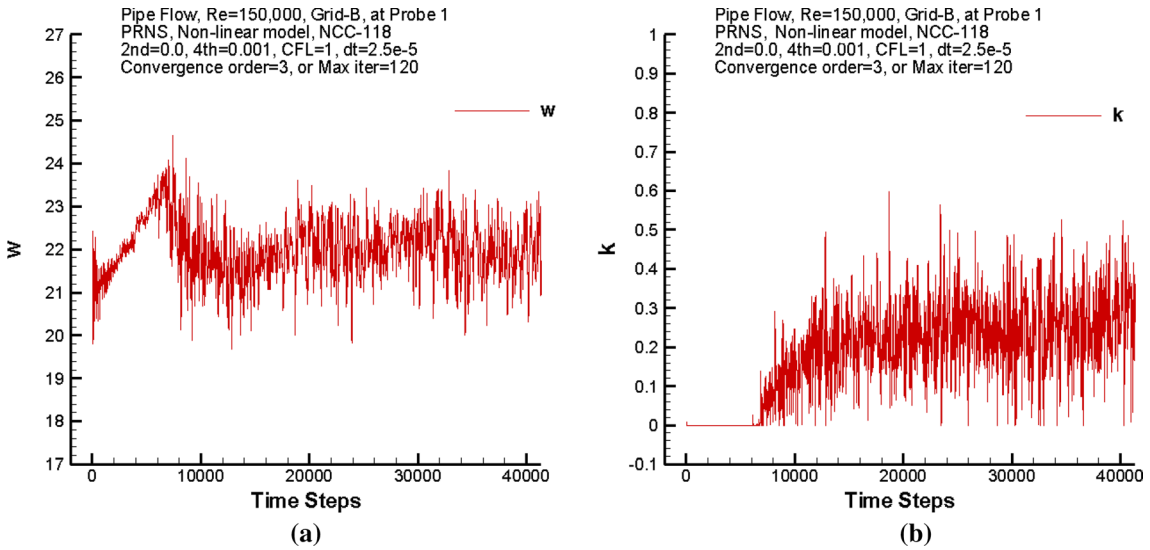

Fig. 6 At Probe 1, the time history of **a** w component; **b** subscale turbulent kinetic energy k

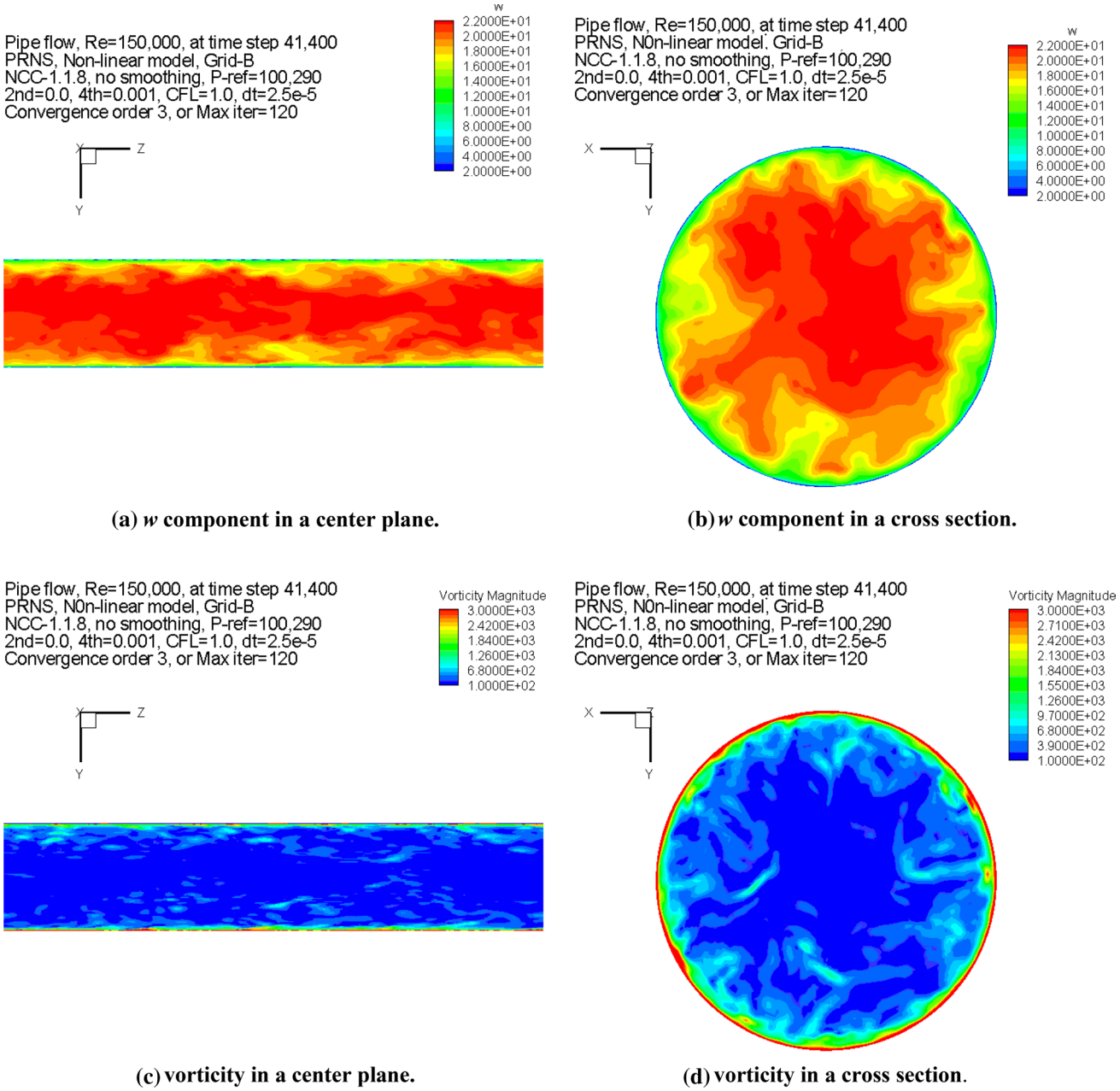

(a) *w* component in a center plane. **(b) *w* component in a cross section.**

(c) vorticity in a center plane. **(d) vorticity in a cross section.**

Fig. 7 Instantaneous contours of various variables in both a center plane and a cross section

velocity and the subscale turbulent kinetic energy k at Probes 1, 6, and 14, which correspond to the locations $r/R = 0.0$, 0.5, and 0.9743, or $y^+ = 3322$, 1661, and 85. Probe 1 is at the center of the pipe, Probe 6 is at the midpoint between the center and the pipe wall, and Probe 14 is very close to the wall. Figure 6 shows the solutions at Probe 1. The solutions at Probe 6 and Probe 14 are shown in Figures A1 and A2 in the electronic supplementary material. The time histories at 28 other locations along the pipe radius and axis are also available. These time histories indicate that the initially induced disturbances of the velocity components are at first somewhat damped, followed by the development of new fluctuations, which are then quickly amplified and evolved into a fully developed turbulent pipe flow. The amplitude of the velocity fluctuations increases from the center toward the wall, so does the subscale turbulent kinetic energy.

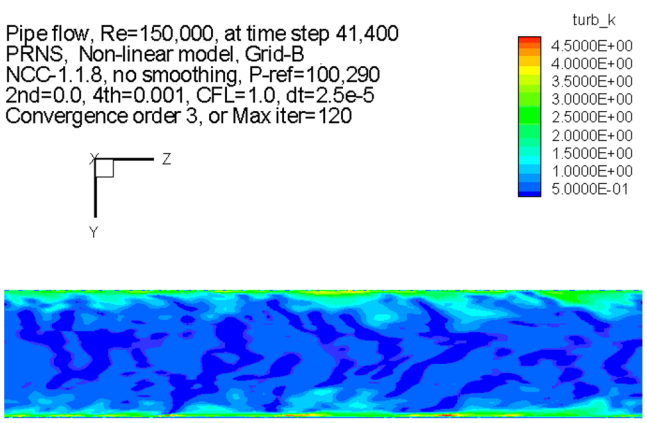

(e) k in a center plane.

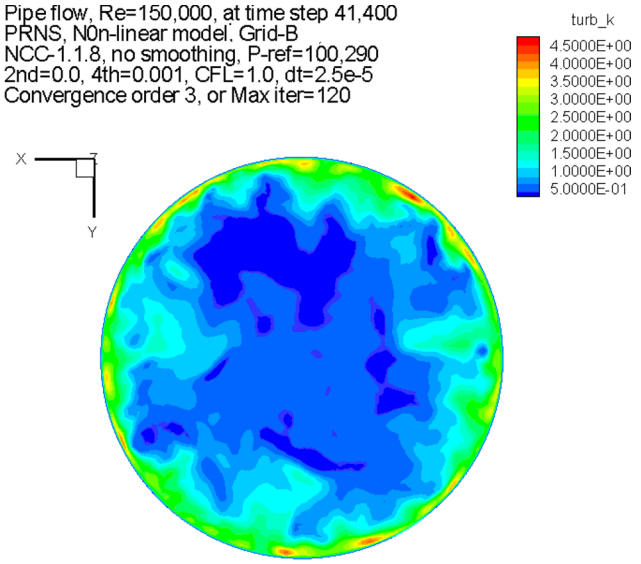

(f) k in a cross section.

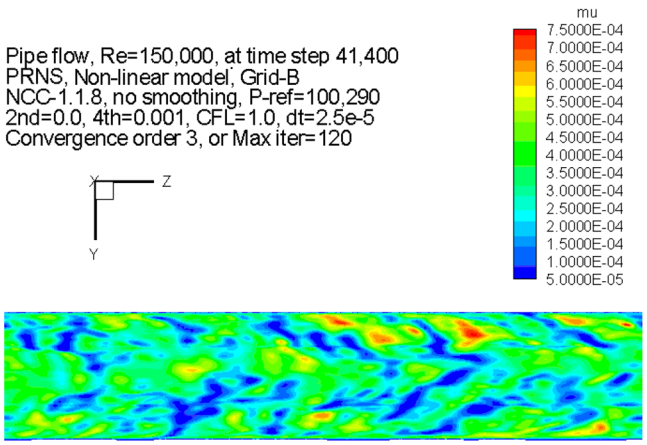

(g) effective viscosity in a center plane.

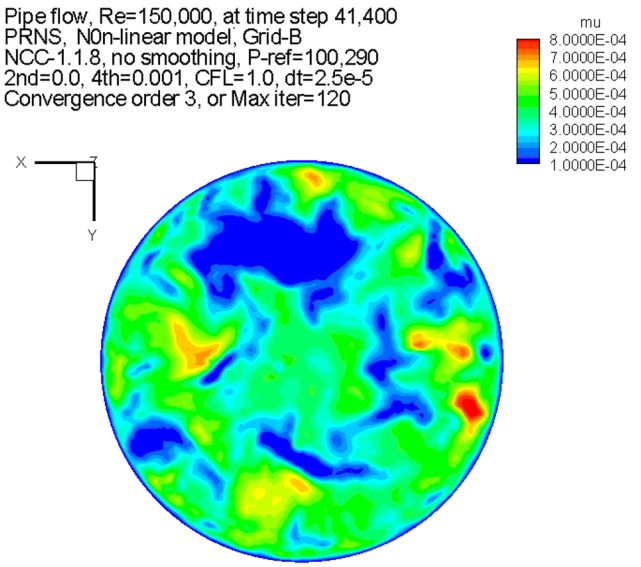

(h) Effective viscosity in a cross section.

Fig. 7 (continued)

3.1.2.2 Instantaneous contour To examine the turbulent flow structures, we have plotted the instantaneous contours of various variables in both a center plane and a cross section. Here we present the instantaneous contours of the axial velocity component, the vorticity magnitude, the subscale turbulent kinetic energy, and the effective subscale viscosity in Fig. 7. The contours of the velocity component and the vorticity magnitude may illustrate the features of the resolved large-scale turbulent structures, whereas the subscale turbulent kinetic energy and the effective viscosity illustrate the highly nonuniform features of the subscale turbulence.

3.1.2.3 Radial profile The radial profiles of various flow variables (w, u, v, gauge pressure, vorticity magnitude, Mach number, subscale turbulent kinetic energy and dissipation rate, effective subscale eddy viscosity) are examined at dif-

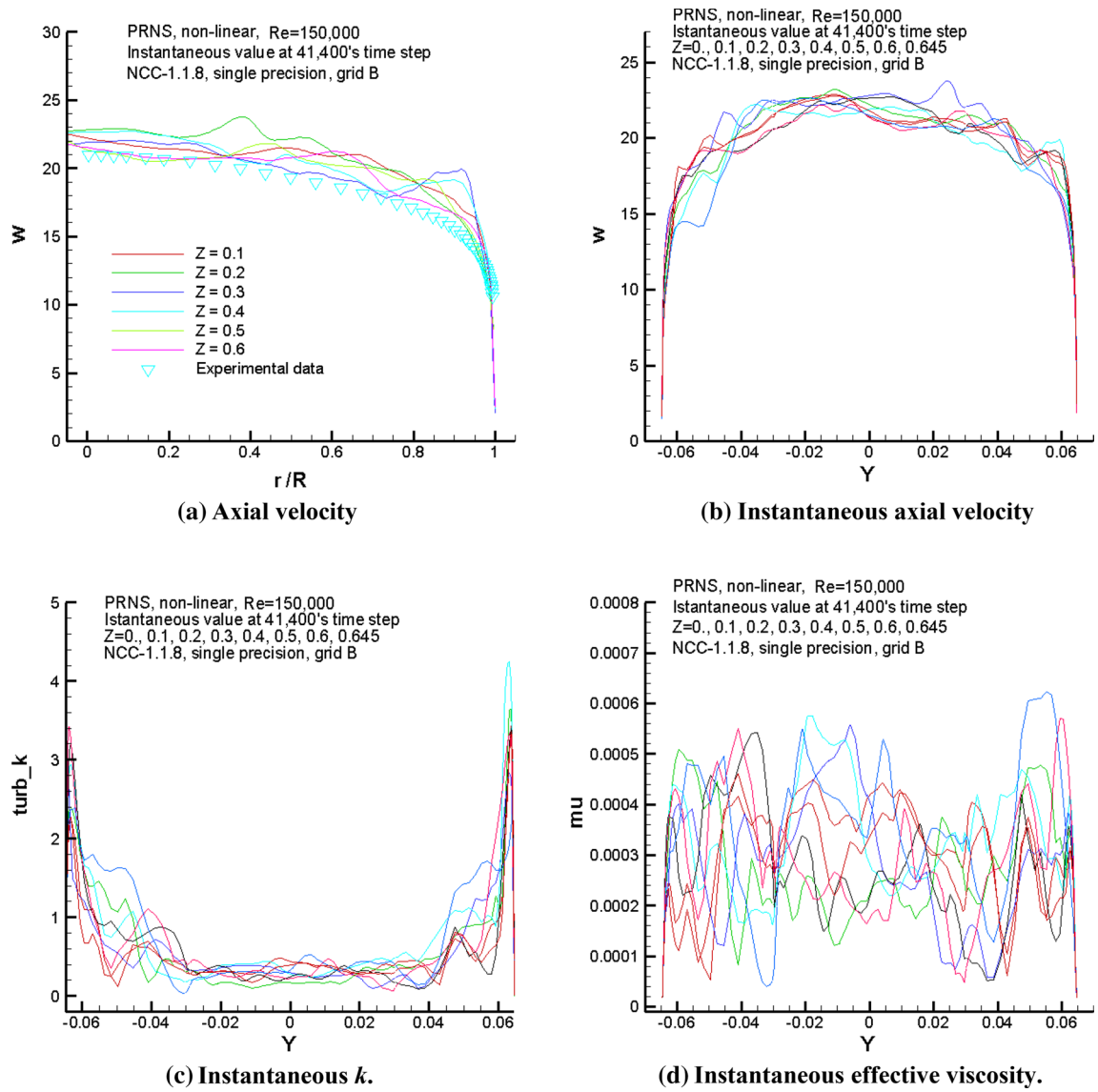

Fig. 8 Radial profiles of various variables

ferent locations along the pipe axis $z = 0.0, 0.1, 0.2, 0.3, 0.4, 0.5, 0.6, 0.645$ for the spatial development of the turbulent flow. Note that z is nondimensionalized by the pipe radius. Figure 8a shows the experimentally measured mean axial velocity [16] together with the (calculated) instantaneous axial velocity at six downstream locations. Figure 8b presents the profiles diametrically. Figure 8c, d illustrates the radial profiles of the subscale turbulent kinetic energy and the effective viscosity, respectively. These results indicate that the simulated turbulent flow is fully developed and is statistically homogeneous along the pipe.

3.1.2.4 Spectrum and correlation analysis Figures 9 and 10 present the power spectrum density (PSD) of the axial velocity component and its two-point (time) correlation at three locations (Probes 1, 6, and 14). The broadband feature of the PSD (i.e., more than two orders of energy variation from small scale to large scale) and the typical two-point correlation shapes (i.e., the correlation rapidly decreases as the time lag increases) indicate that the TFNS/VLES simulation with RCP = 0.16 does mimic the statistical features of a fully developed turbulence.

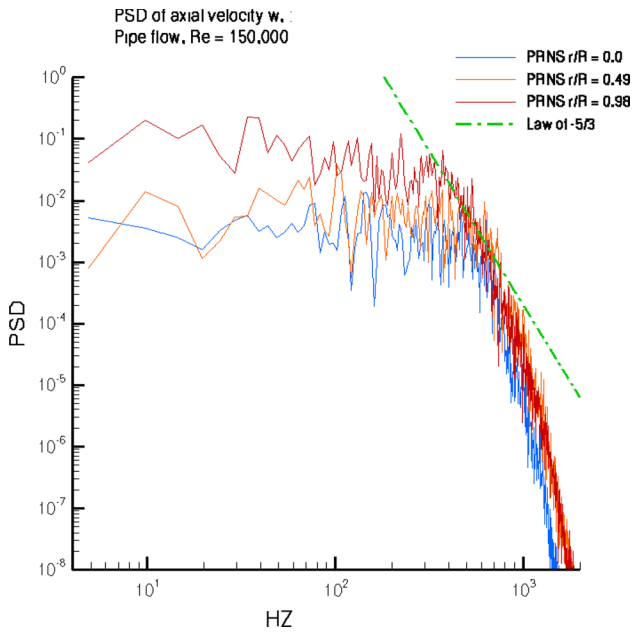

Fig. 9 Power spectrum density of the axial velocity at Probes 1, 6, and 14

The experimental data of the mean axial velocity at Reynolds number of 145,700 are used to compare the time-averaged axial velocity obtained from the current simulation at a Reynolds number of 150,000. In Fig. 11, the result obtained from URANS (unsteady Reynolds-averaged Navier–Stokes) using a standard k–ε model and the wall function is included. The result obtained from TFNS/VLES is in a reasonable agreement with the experimental data, while the URANS result exhibits significant under-prediction.

3.2 Flow in a single-element LM6000 injector

LM6000 is a General Electric low NOx gas turbine. We have performed several types of numerical simulations of turbulent flows issued from one of its fuel injectors. A highly swirling jet is injected from a circular inlet. The inlet pressure is about 6 atm, and the inlet temperature is about 644 K. The inlet boundary conditions are based on the experimental data. The combustor is a rectangular box. The Reynolds number based on the inlet axial velocity and the inlet jet diameter is about 3,200,000. Figure 12 depicts the computational domain and the numerical grid. The total number of grid points is about 495,000, which is the grid used for all simulations with the approaches of TFNS/VLES, URANS, and RANS. Here we will only present the results from the TFNS/VLES approach.

The value of RCP is set to 0.18. A convective unsteady boundary condition [19], which is similar to the one proposed by Ferziger [20] and Grinstein et al. [21], is applied at the outlet boundary. The initial condition is set with a solution of a steady RANS simulation (see Figs. 13, 14). Two subscale models (nonlinear and linear) have been used. The results indicate that the nonlinear subscale models are very helpful for capturing large-scale swirling turbulent flow structures.

3.2.1 Nonlinear subscale model

The time histories of velocity components and gauge pressure are recorded at four locations along the centerline: $x = 0.015$, 0.05, 0.10, and 0.2 m, from which we may monitor the development of turbulent fluctuations. Here, the

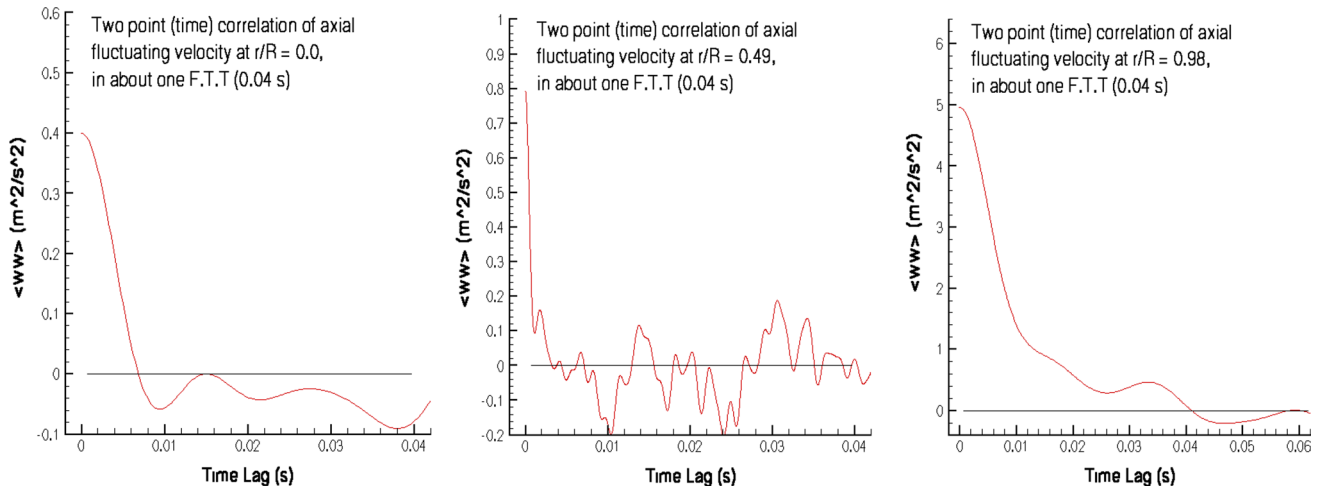

Fig. 10 Two-point time correlations of <*ww*> at Probes 1, 6, and 14

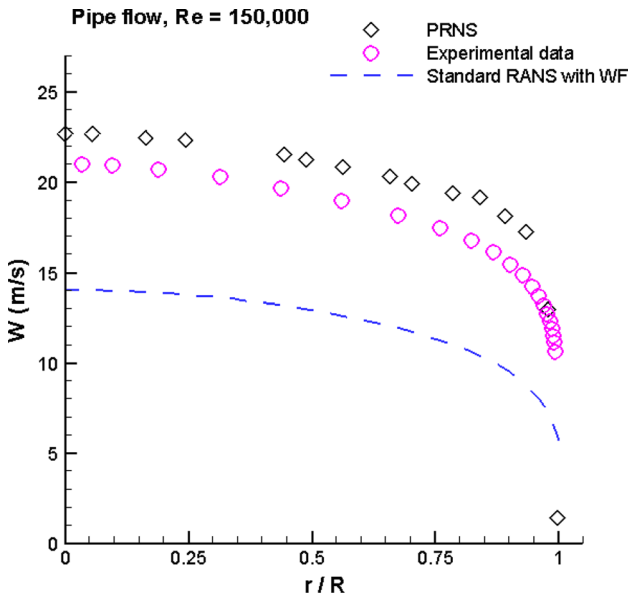

Fig. 11 Comparison of mean axial velocity between TFNS/VLES, URANS, and experimental data

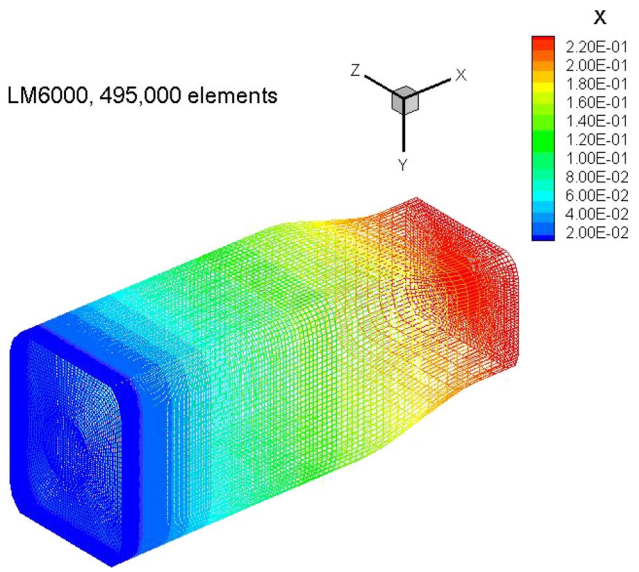

Fig. 12 Computational domain for LM6000 single injector flow simulation

presented time histories of the velocity components are at $x = 0.1$ and 0.2 m, which are located before and after the rear stagnation point of the recirculation zone. Figures 15 and 16 indicate that the turbulent fluctuations are fully developed.

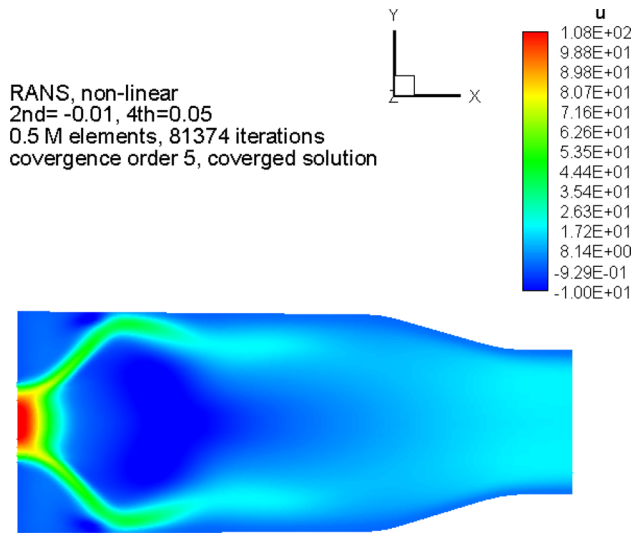

Fig. 13 Contour of the axial velocity (RANS)

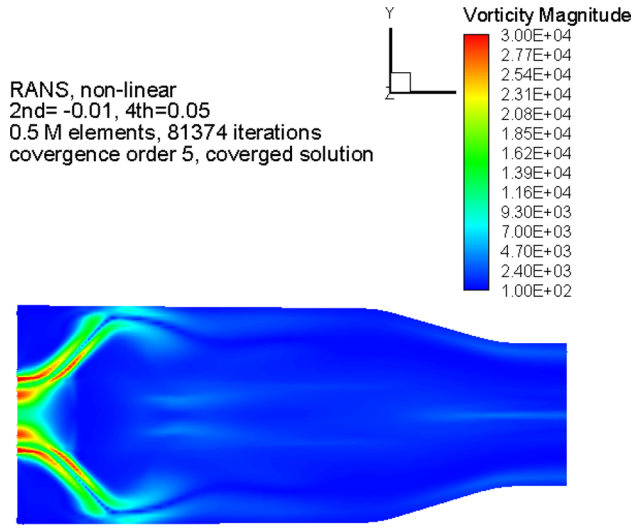

Fig. 14 Contour of the vorticity magnitude (RANS)

The instantaneous contours of flow variables in a center plane are presented for the time-step of 60,000, which is about 100 times of the through flow time (TFT, defined as the ratio of the length of the combustor to the inlet centerline axial velocity). Figures 17 and 18 are the contours of the axial velocity and the vorticity magnitude, respectively. The recirculation zone, the massive separation, and the shear layers are clearly visualized.

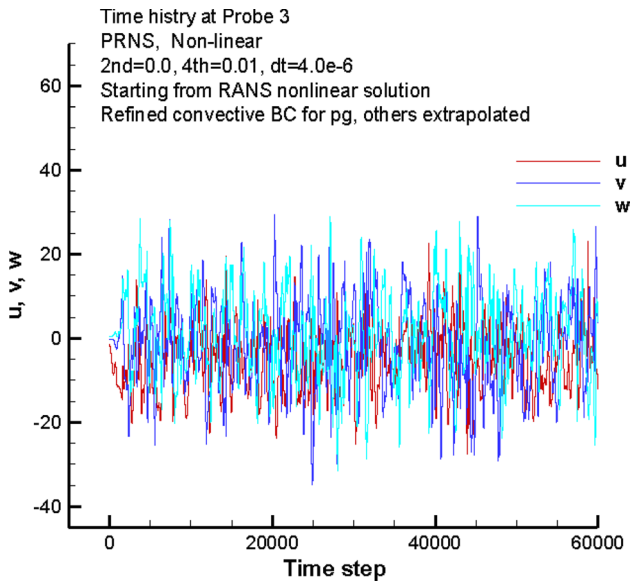

Fig. 15 Time histories of velocity at Probe 3

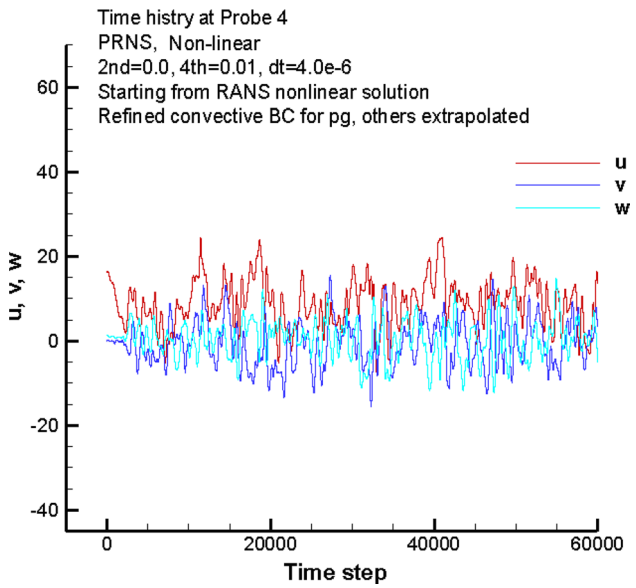

Fig. 16 Time histories of velocity at Probe 4

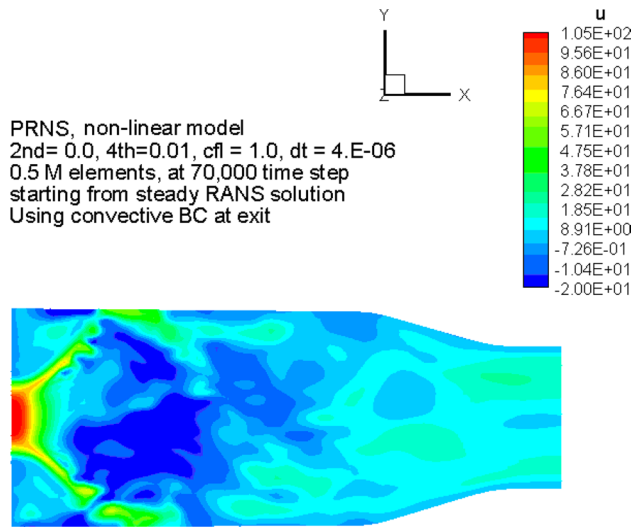

Fig. 17 Contour of instantaneous axial velocity

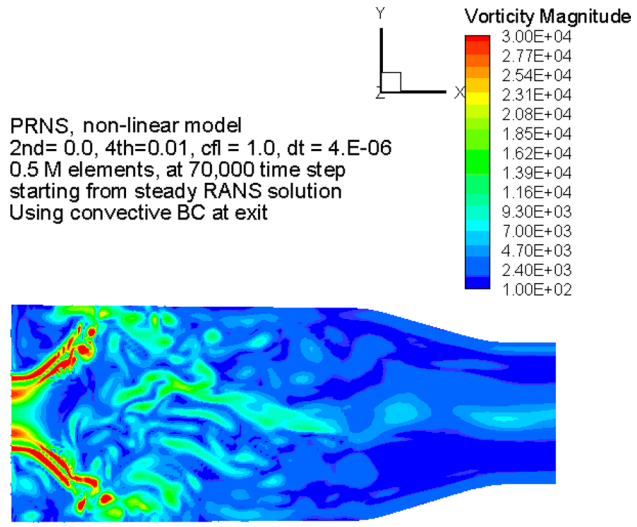

Fig. 18 Contour of instantaneous vorticity

3.2.2 Linear subscale model

In the early stage of the simulation, the calculated turbulent structures look reasonable. However, they are not sustainable in the long run and the calculation crashes after 18,000 time-steps (about 36 times of the through flow time, TFT).

Here, we present the instantaneous contours at two instances: the time-step of 10,000 (about 20 TFT) and the time-step of 18,000 (about 36 TFT). Around 20 TFT, the flow structures, shown in Figs. 19a, 20a, and 21a, look reasonable except for the subscale turbulent quantities. The subscale turbulent kinetic energy k (not shown) and the eddy viscosity μ_T are too small (about two orders of magnitude smaller) when compared to its counterpart

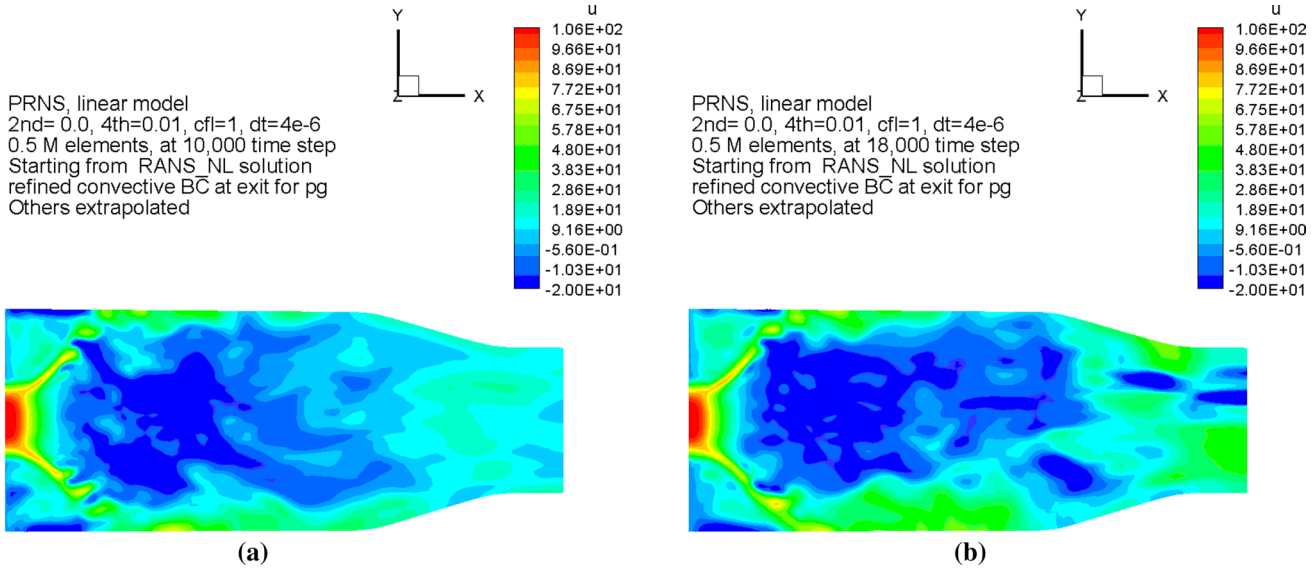

Fig. 19 Axial velocity at **a** 10,000 time-steps; **b** 18,000 time-steps

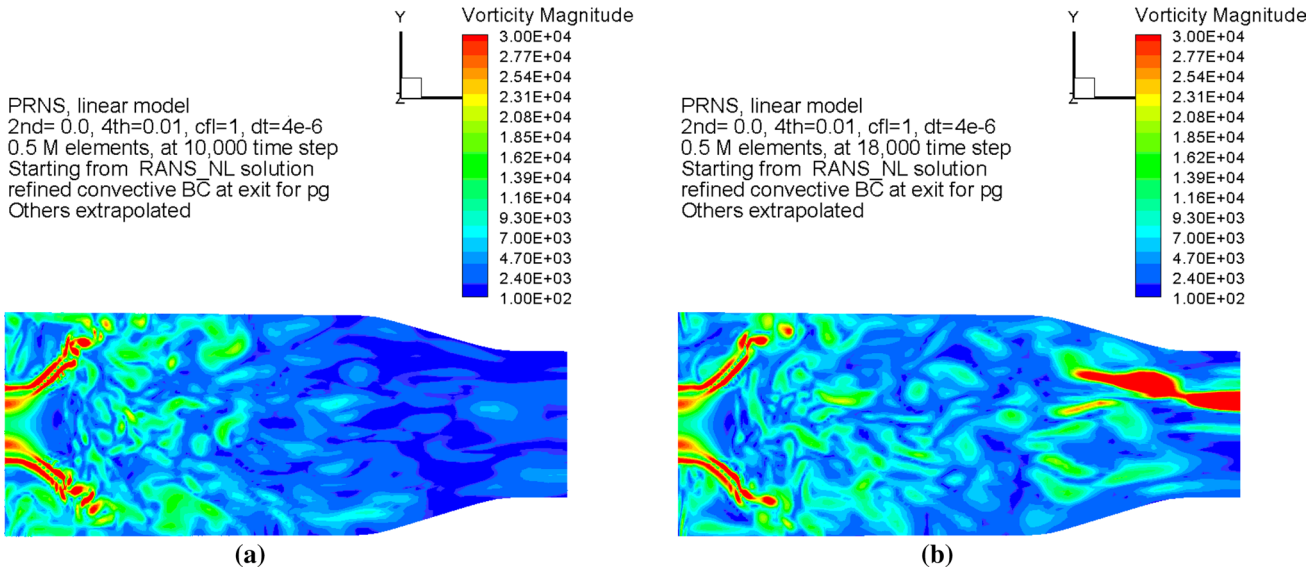

Fig. 20 Contour of vorticity at **a** 10,000 time-steps; **b** 18,000 time-steps

obtained from the nonlinear subscale model. Around 36 TFT, the flow structures near the outlet become unphysical (see Figs. 19b, 20b, 21b), e.g., large amount of high-speed inflows occurs at the exit. The subscale turbulent kinetic energy (not shown) and the eddy viscosity become even weaker and smaller. The simulation crashes soon after 36 TFT. These results suggest that the linear subscale k–ε model does not work very well for high swirling turbulent flows.

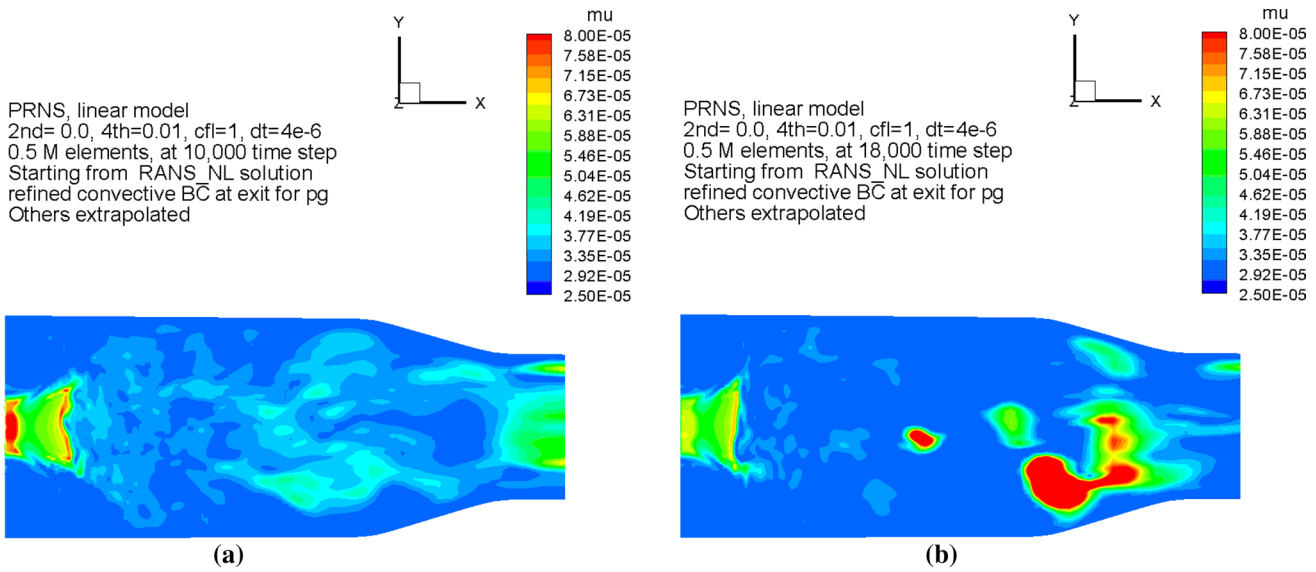

Fig. 21 Effective viscosity at **a** 10,000 time-steps; **b** 18,000 time-steps

3.3 Flow in a single-element LDI combustor

The lean direct injection (LDI) injector is a liquid fuel injector developed to reduce aircraft emissions. Stable combustion is essentially completed within a short distance through rapid fuel and air mixing. This design also allows for the integration of many small fuel injectors into modules facilitating different fuel staging strategies, such as the one shown in Fig. 22. So far, experimental observations have not fully clarified the dynamics of the mixing and combustion processes occurring in these injectors, and numerical studies need to be conducted to achieve a better understanding of the underlying unsteady physics of the LDI combustor.

A very large eddy simulation (TFNS/VLES) has been carried out for the nonreacting turbulent flow in a single-element LDI combustor as the first step toward the simulation of, for example, a 3×3 injector module.

Figure 23 depicts the single-element LDI combustor geometry and its computational domain. The numerical grid is formed using hexahedral elements, and the total number of elements is 862,000, which is a relatively coarse grid used in a previous RANS simulation [22]. Embedded in this figure are the instantaneous iso-surface of zero axial velocity component colored by the subscale effective viscosity and six instantaneous streamlines originating from the inlet of the injector, then passing through the swirler and the convergent-divergent nozzle, and finally entering the combustion chamber.

In this study, we first carry out a steady RANS simulation to provide the initial flow field for the TFNS/VLES simulation. The inlet boundary conditions are set by specifying the velocity, the density, and the temperature based on the experimental data, and the outlet boundary condition is an unsteady convective boundary condition [19]. The nonlinear subscale model is used since it has been proven to be very effective in our previous studies. The value of RCP is set to 0.25 since the available numerical grid spacing is very coarse. We have also carried out an unsteady RANS (URANS) simulation to compare with the TFNS/VLES simulation. Available experimental data are used to assess the simulation results. It is demonstrated that, even with a grid spacing used in RANS, the TFNS/VLES approach can successfully reveal the complex unsteady turbulent structures that occurred in this single-element LDI combustor. These dynamically important flow structures include the precessing vortex core (PVC) and the vortex breakdown bubble (VBB). Good comparisons of velocity components with the experimental data are also demonstrated.

3.3.1 Flow structures

In the following, the instantaneous contour plots and the iso-surfaces of some quantities are used to illustrate the flow structures.

3.3.1.1 Instantaneous contour plots Figure 24 is the contour plot of the axial velocity component in a center plane at time-step of 90,000. It shows that a strong recirculation zone is extended from the combustor dump plane deep into the upstream nozzle throat. Figure 25 is the contour plot of

Fig. 22 Configuration of a 3×3 LDI injector module

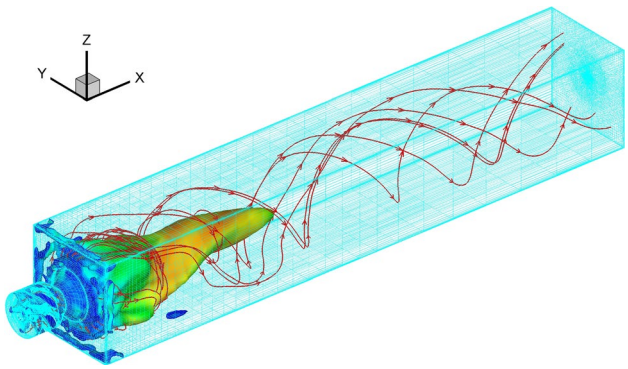

Fig. 23 A snapshot of the flow and the grid spacing

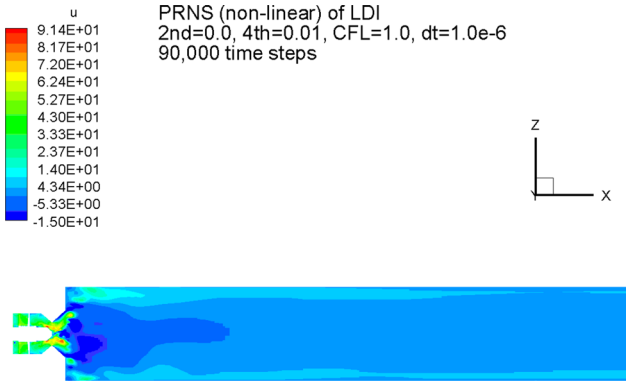

Fig. 24 Contour of axial velocity in a center plane

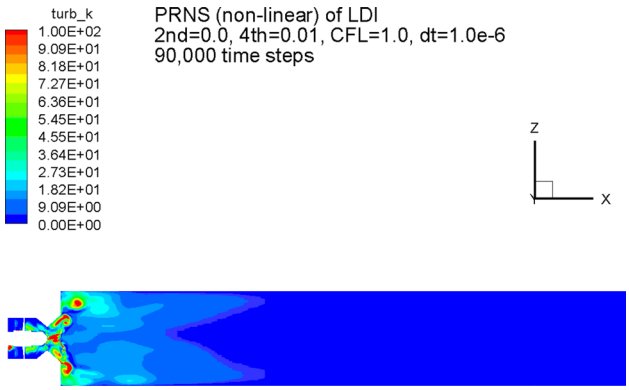

Fig. 25 Contour of subscale k in a center plane

the subscale turbulent kinetic energy, which is high near the high-shear regions.

3.3.1.2 Instantaneous PVC and VBB The dominant flow structures in the LDI combustor can be best visualized via the iso-surface of the zero axial velocity and the iso-surface of a relatively low pressure. The iso-surface of the zero axial velocity is also known as the vortex breakdown bubble (VBB). The iso-surface of a sufficiently low pressure captures the precessing vortex core (PVC). Figures 26 and 27 are the snapshots taken from two different angles. Figure 26 is a side view, and Fig. 27 is a perspective view. In these figures, the dark blue region is a vortex core, which is formed near the nozzle throat and extends into the combustor chamber. This spiraling vortex rotates and breaks; it changes randomly in space and time. Embedded in these figures is an instantaneous streamline, which starts from the inlet of the injector and goes through a complex seemingly random path in the combustor chamber. This streamline spirals around the dark blue surface indicating that the dark blue region is indeed a vortex core. The light green surfaces are the iso-surfaces of the zero axial velocity.

3.3.2 Profiles of velocity components

The experimental data reported in [23] are used to assess the current numerical results. The experimental data are mean values, but the numerical results are instantaneous values.

3.3.2.1 Axial velocity distribution along the centerline Figure 28 is a comparison of the axial velocity profile between the calculated instantaneous values and the experimental mean value. Figure 29 is an enlarged view near the dump plane of the combustor chamber. These figures show that the calculated values are in reasonable agreement with the experimental data. It also supports the experimental observation that, near the dump plane, the turbulent fluctuations are quite large.

3.3.2.2 Axial velocity distribution along the *y*-axis at several downstream locations The distributions of the axial

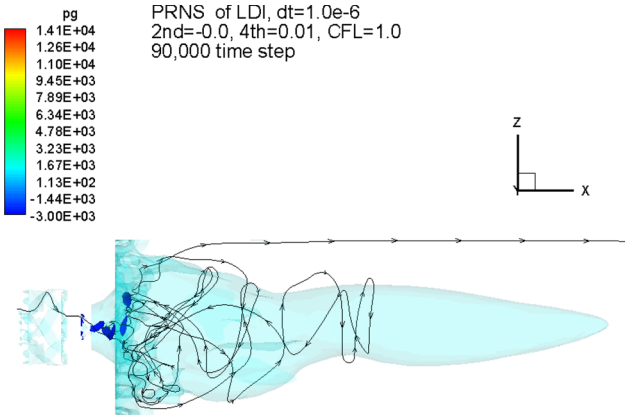

Fig. 26 Side view of the PVC and the VBB

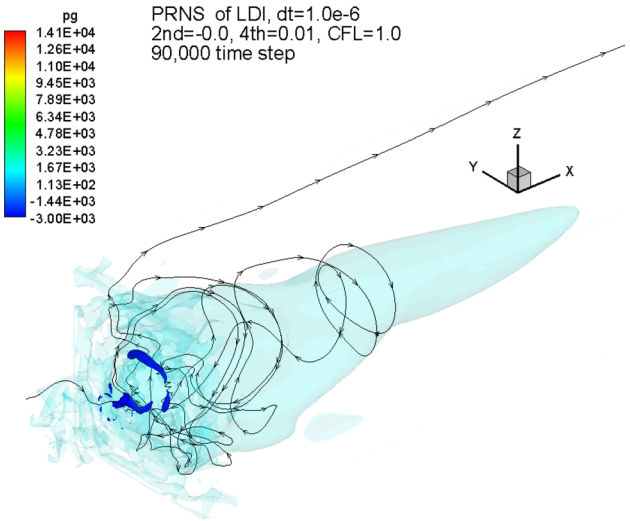

Fig. 27 45° view of the PVC and the VBB

velocity along the y-axis in the cross-section plane at several downstream locations $x=3$ mm, 6 mm, 9 mm, 12 mm, 90 mm, and 180 mm are presented for 10 different instances and compared with the experimental mean value. Figure 30a–c clearly indicates that the turbulent fluctuations are quite large near the inlet of the combustion chamber and are quickly reduced toward downstream as shown in Fig. 30d–f. In addition, the largest turbulent fluctuations are off the centerline, somewhere between the centerline and the wall.

3.3.2.3 Velocity components *w* and *v* along the *y*-axis at several downstream locations The distributions of the other two velocity components w and v along the y-axis in the cross section at several downstream locations $x=3$ mm, 6 mm, 9 mm, 12 mm, 15 mm, and 90 mm are shown for 10 different

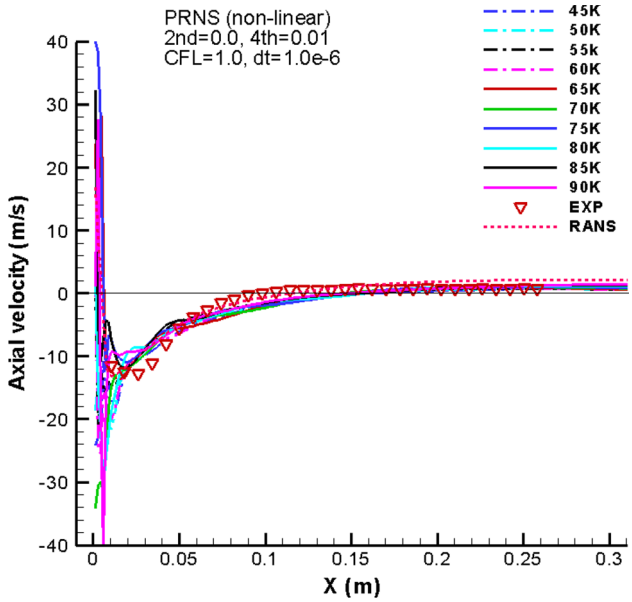

Fig. 28 Centerline profile of the axial velocity

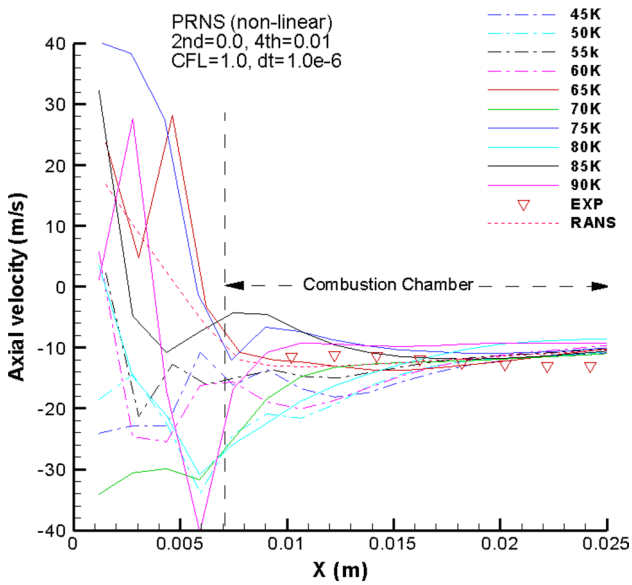

Fig. 29 Instantaneous profiles near the dump plane

instances and compared with the experimental mean value in Fig. 31 and Figure A3 in the electronic supplementary material, respectively. Again, these figures clearly indicate that the turbulent fluctuations are larger near the inlet of the combustor chamber and are quickly reduced downstream. The strongest turbulent fluctuations are found off the centerline, somewhere between the centerline and the wall.

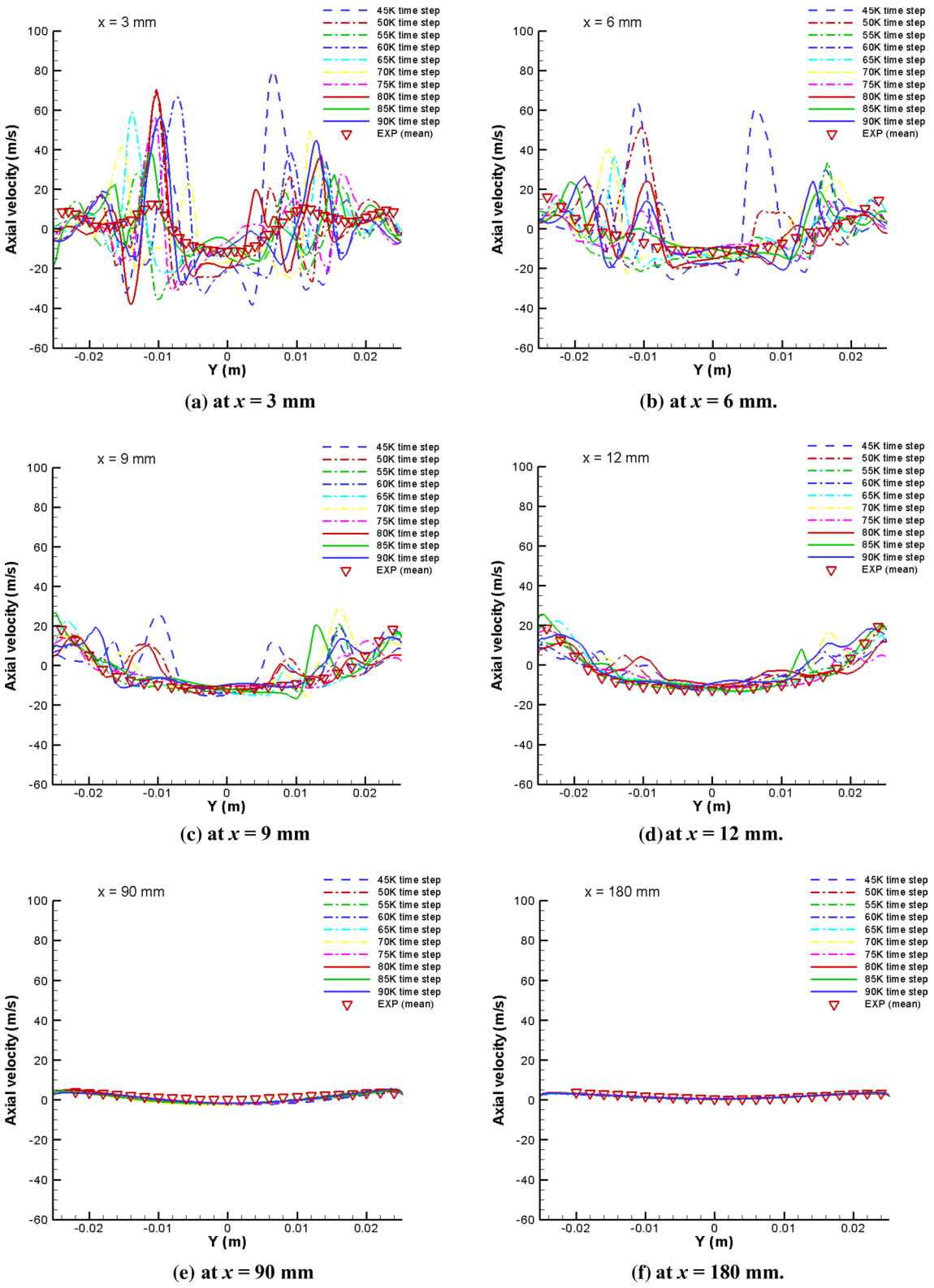

Fig. 30 Axial velocity along the *y*-axis at several downstream locations

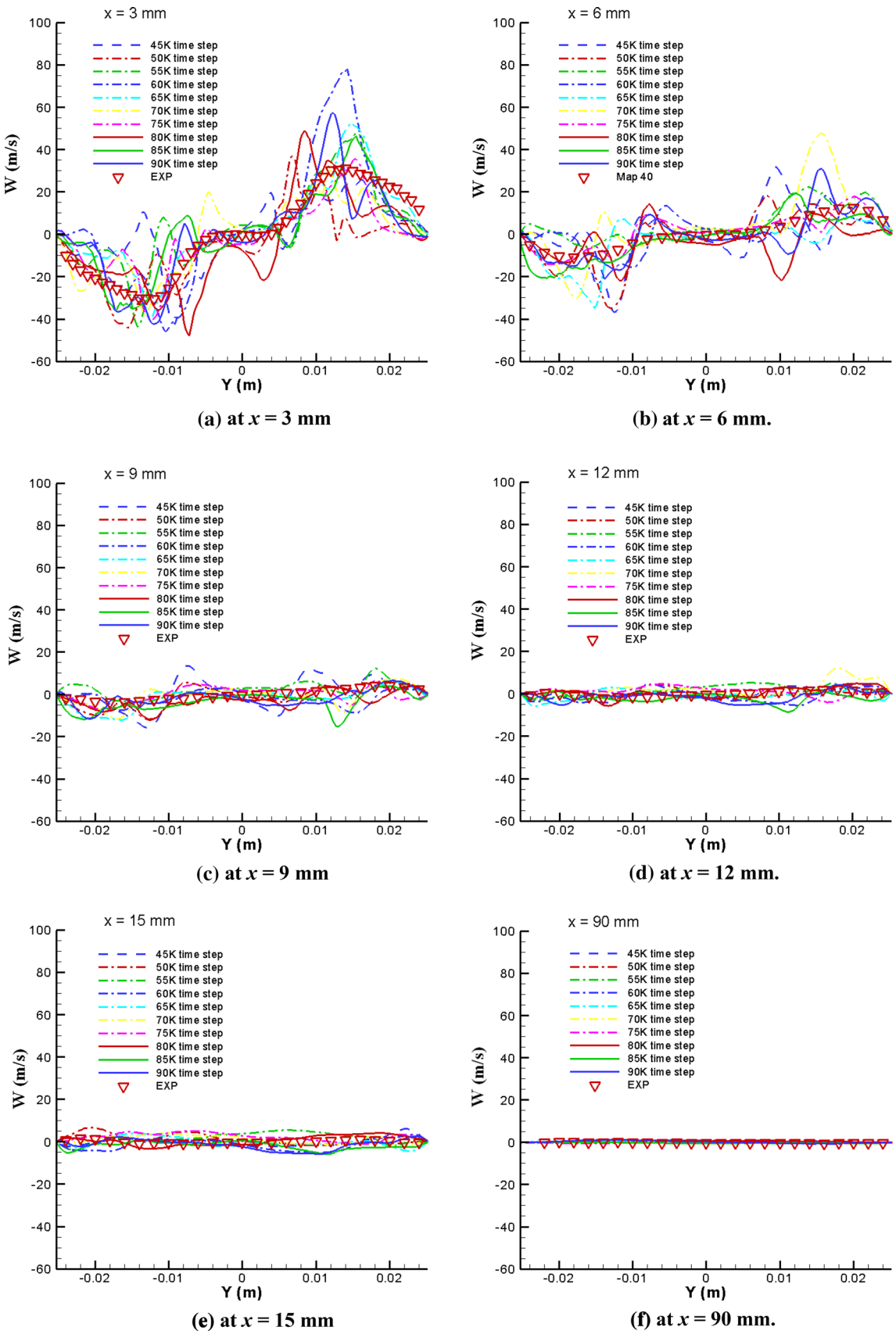

Fig. 31 Velocity component w along the y-axis in the cross section at several downstream locations

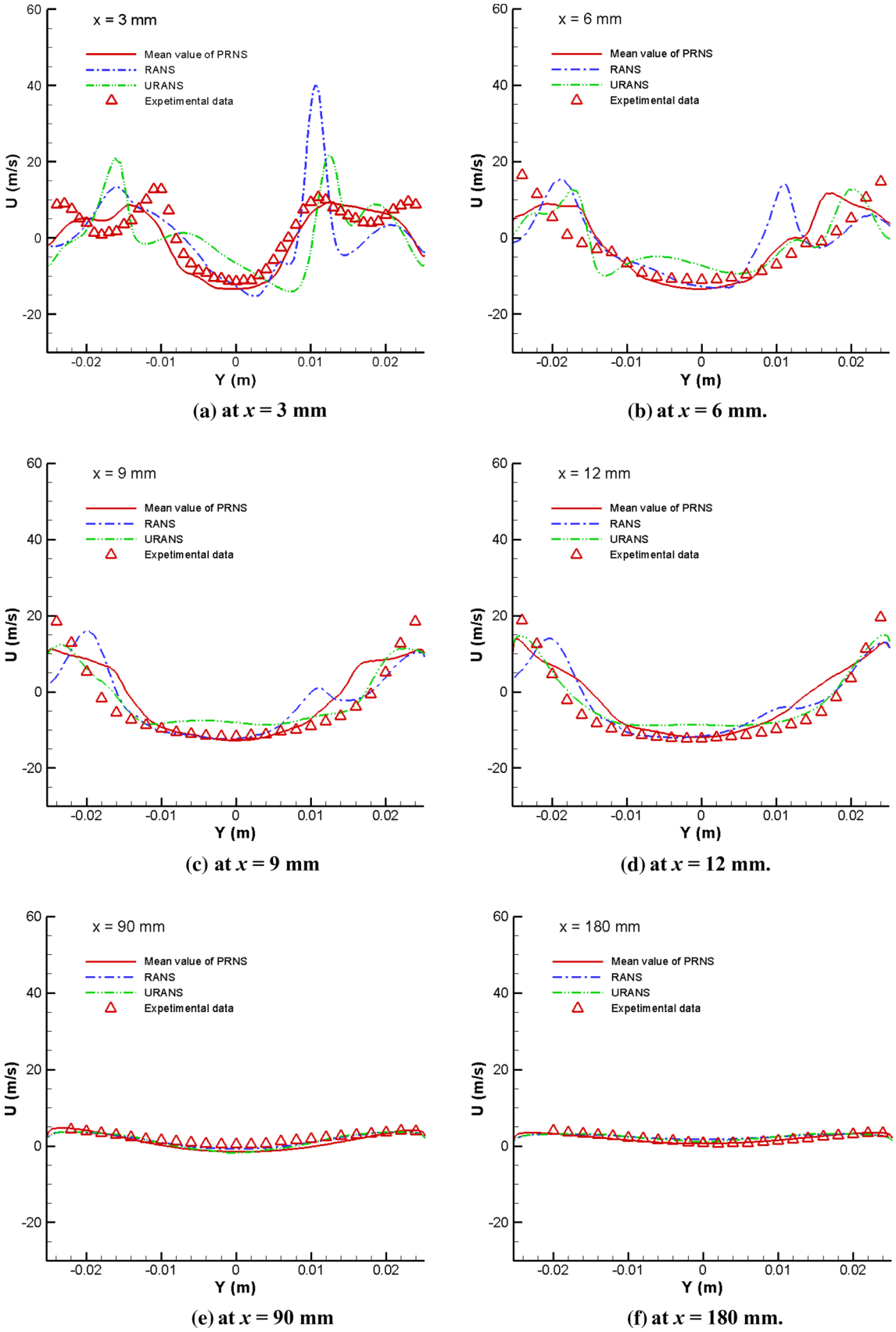

Fig. 32 Axial mean velocity U along the y-axis in the cross-section plane at several locations

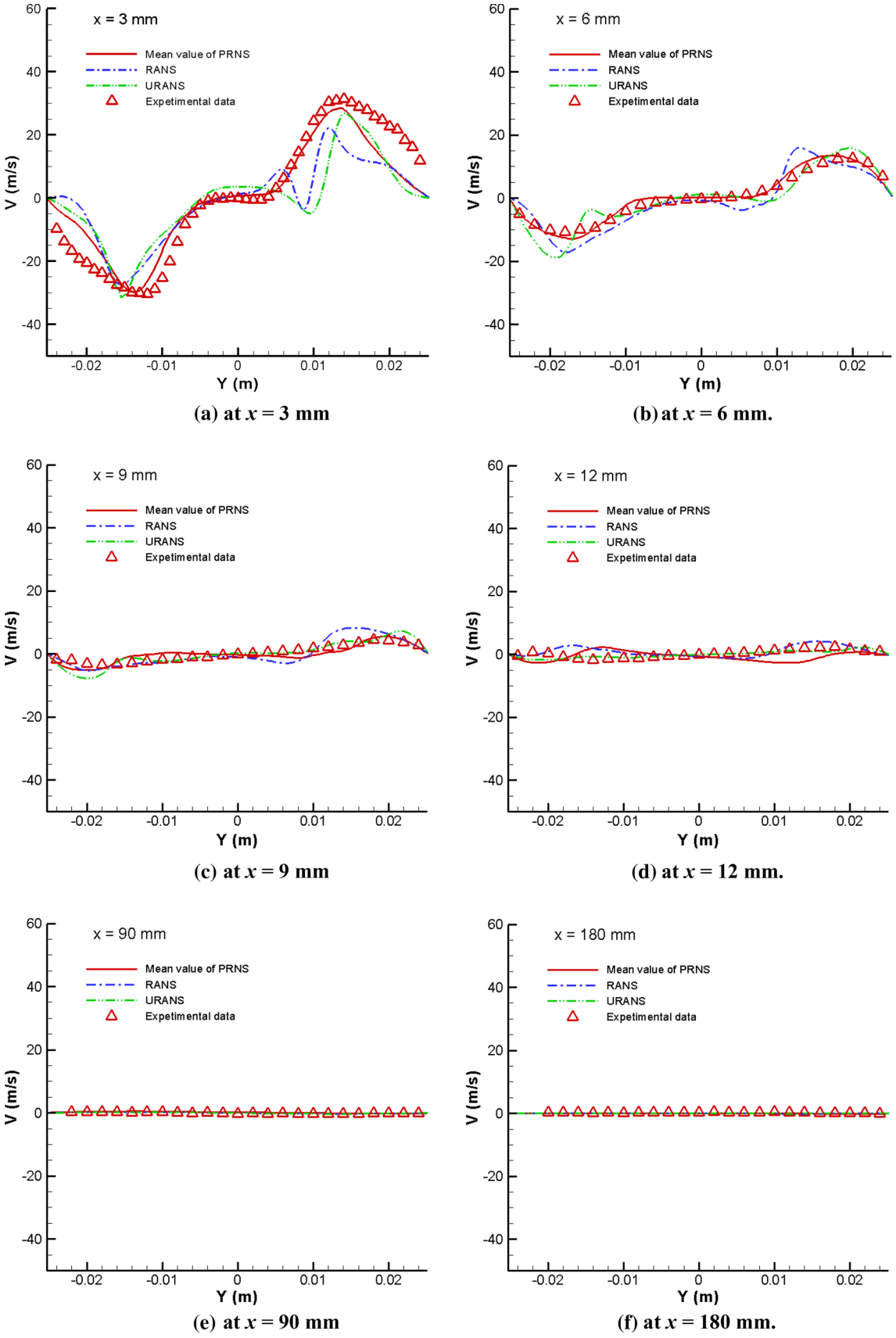

Fig. 33 Mean velocity components V along the y-axis in the cross section at several downstream locations

3.3.3 Comparisons between RANS, URANS, TFNS/VLES, and experimental data

This section will compare the time-averaged mean velocity profiles from TFNS/VLES, URANS, and RANS simulations with the experimental data. The mean values are obtained by time-averaging the TFNS/VLES and URANS simulations over the last 10,000 time-steps.

3.3.3.1 Axial mean velocity *U* along the *y*-axis at several downstream locations The distributions of the axial mean velocity U along the y-axis in the cross-section plane at several downstream locations $x=3$ mm, 6 mm, 9 mm, 12 mm, 90 mm, and 180 mm are presented for RANS, URANS, and TFNS/VLES compared with the experimental mean values. Figure 32 clearly shows that the time-averaged axial velocity profile from TFNS/VLES simulation is much closer to the experimental data, especially in the region near the inlet of the combustor chamber where turbulent fluctuations are strong.

3.3.3.2 Mean velocity components *V* and *W* along the *y*-axis at several downstream locations The distributions of the other two mean velocity components V and W along the y-axis in the cross-section at several downstream locations $x=3$ mm, 6 mm, 9 mm, 12 mm, 15 mm, and 90 mm are compared with the experimental mean value in Fig. 33 and Figure A4 in the supplementary material, respectively. Again, these figures clearly indicate that the time-averaged mean velocity profiles from TFNS/VLES simulation are much closer to the experimental data, especially in the region near the inlet of the combustor chamber where turbulent fluctuations are strong.

4 Conclusions

The basic equations of the TFNS/VLES approach for large or very large simulations are presented. They are based on the time-filtering with a constant filter width. Consequently, they are grid spacing independent or grid invariant. This feature allows the possibility of achieving a grid-independent solution.

The nonlinear subscale models are of better mathematical and physical meanings than the linear eddy viscosity models. The advantage of the nonlinear subscale models over the linear eddy viscosity models has been demonstrated in the simulations of turbulent pipe flow at low Reynolds number $\mathrm{Re}_\tau=180$ and the high swirling flow issued from an LM6000 single injector. In both cases, the linear eddy viscosity model does not lead to a sustainable and physically meaningful solution.

The simulations of the single-element LDI injector flow using the nonlinear subscale model have demonstrated that the TFNS/VLES approach can capture the dynamically important unsteady turbulent structures even with a grid spacing typically used for the RANS calculation. This is particularly encouraging, because the capability of predicting unsteady turbulent flow structures with a coarse grid is very much desired for practical engineering applications.

Acknowledgements This work is supported by the NASA Fundamental Aeronautics Program. The authors would like to thank Farhad Davoudzadeh for providing the numerical grid of the single-element LDI combustor. Authors would also like to thank Andrew Higgins and Chin-Hao Chang for their critical comments and detailed advice to our manuscript.

References

1. Liu, N.-S., Shih, T.-H.: Turbulence modeling for very large-eddy simulation. AIAA J. **44**(4), 687–697 (2006). https://doi.org/10.2514/1.14452
2. Shih, T.-H., Liu, N.-S.: Modeling of internal reacting flows and external static stall flows using RANS and TFNS. Flow Turbul. Combust. **81**, 279–299 (2008). https://doi.org/10.1007/s10494-007-9097-z
3. Davidson, L., Peng, S.H.: Hybrid LES–RANS modelling: a one-equation SGS model combined with a k–ω model for predicting recalculating flows. Int. J. Numer. Methods Fluids **43**, 1003–1018 (2003). https://doi.org/10.1002/fld.512
4. Larsson, J., Lien, F.S., Yee, E.: The artificial buffer layer and the effect of forcing in hybrid LES/RANS. Int. J. Heart Fluid Flow **28**, 1443–1459 (2007). https://doi.org/10.1016/j.ijheatfluidflow.2007.04.007
5. Spalart, P.R., Jou, W.H., Allmaras, S.R.: Comments on the feasibility of LES for wings and on a hybrid RANS/LES approach. In: Advances in DNS/LES. Greyden Press, Dayton (1997)
6. Fasel, H.F., von Terzi, D.A., Sandberg, R.D.: A methodology for simulating compressible turbulent flows. J. Appl. Mech. **73**, 405–412 (2005). https://doi.org/10.1115/1.2150231
7. Cabot, W., Moin, P.: Approximate wall boundary conditions in the large-eddy simulation of high Reynolds number flow. Flow Turbul. Combust. **63**, 269–291 (2000). https://doi.org/10.1023/A:1009958917113
8. Sagaut, P.: Large Eddy Simulation for Incompressible Flows. Springer, Berlin (2006). https://doi.org/10.1007/b137536
9. Shih, T.-H.: Constitutive relations and realizability of single-point turbulence closures. In: Hallback, M., Henningson, D.S., Johansson, A.V., Alfredsson, P.H. (eds.) Turbulence and Transition Modelling, Chapter 4. Kluwer, Dordrecht (1996). https://doi.org/10.1007/978-94-015-8666-5_4
10. Shih, T.-H.: Mathematical modeling of turbulent flows. In: Daiguji, H., Miyake, Y., Kasagi, N. (eds.) Fluid Dynamics Research, vol. 20. Elsevier Science B.V. (1997)
11. Smagorinsky, J.: General circulation experiments with the primitive equations. Mon. Weather Rev. **91**(3), 99–165 (1963). https://doi.org/10.1175/1520-0493(1963)091%3C0099:GCEWTP%3E2.3.CO;2
12. Kim, W.-W., Menon, S., Mongia, H.C.: Large eddy simulation of gas turbine combustor flow. Combust. Sci. Technol. **143**, 25–62 (1999). https://doi.org/10.1080/00102209908924192

13. Shih, T.-H., Zhu, J., Liou, W., Chen, K-H., Liu, N-S., Lumley, J.L.: Modeling of Turbulent Swirling Flows. NASA/TM-113112 (1997)
14. Shih, T.-H., Liou, W.W., Shabbir, A., Yang, Z., Zhu, J.: A new k–ε eddy viscosity model for high Reynolds number turbulent flows. Comput. Fluids **24**(3), 227–238 (1995). https://doi.org/10.1016/0045-7930(94)00032-T
15. Tennekes, H., Lumley, J.L.: A First Course in Turbulence. MIT Press, Cambridge (1972)
16. Zagarola, M., Smits, A., Orszag, S., Yakhot, V.: Experiments in high Reynolds number turbulent pipe flow. 34th Aerospace Sciences Meeting and Exhibit, Reno, NV, AIAA Paper 1996-654 (1997). https://doi.org/10.2514/6.1996-654
17. Shih, T.-H., Liu, N.-S.: Assessment of the Partially Resolved Numerical Simulation (TFNS) approach in the National Combustion Code (NCC) for Turbulent Nonreacting and Reacting Flows, NASA/TM 2008-215418
18. Shih, T.-H., Povinelli, L.A., Liu, N.-S.: Application of generalized wall function for complex turbulent flows. J. Turbul. **4**, n15 (2003). https://doi.org/10.1088/1468-5248/4/1/015
19. Shih, T.-H., Liu, N.-S.: Numerical Study of Outlet Boundary Conditions for Unsteady Turbulent Internal Flows Using the NCC, NASA/TM-2009-215486
20. Ferziger, J.H., Perić, M.: Computational Methods for Fluid Dynamics. Springer, Berlin (1996). https://doi.org/10.1007/978-3-642-56026-2
21. Grinstein, F.F., Oran, E.S., Boris, J.P.: Pressure field, feedback, and global instabilities of subsonic spatially developing mixing layers. Phys. Fluids A **3**(10), 2401–2409 (1991). https://doi.org/10.1063/1.858178
22. Davoudzadeh, F., Liu, N.-S., Moder, J.P.: Investigation of swirling air flows generated by axial swirls in a flame tube. Proceedings of GT2006 ASME Turbo Expo 2006: Power for Land, Sea, and Air May 8–11, 2006 Barcelona, Spain. https://doi.org/10.1115/gt2006-91300
23. Cai, J., Jeng, S.-M., Tacina, R.: The structure of a swirl-stabilized reacting spray issued from an axial swirler. 43rd AIAA Aerospace Science Meeting and Exhibit, Reno, NV, AIAA Paper 2005-1424 (2005). https://doi.org/10.2514/6.2005-1424